Hybrid RANS/LES Simulations and Aeroacoustic Analysis of Jet Flows using an hp-Adaptive Discontinuous Galerkin Method

Francesca Basile, Jean-Baptiste Chapelier, Romain Laraufie, Pascal Frey

Hybrid RANS/LES simulations and aeroacoustic analysis of jet flows using an *hp*-adaptive discontinuous Galerkin method

Francesca Basile[1,2,3*], Jean-Baptiste Chapelier[1], Romain Laraufie[2] and Pascal Frey[3]

[1]ONERA - Université Paris-Saclay, Departement of Aeroelasticity, Aerodynamics Aeroacoustics, Châtillon, 92322, France.
[2]Airbus Operations SAS, Flight Physics Capabilities, Toulouse, 31060, France.
[3]Sorbonne Université, Laboratoire Jacques Louis Lions, Paris, 75005, France.

*Corresponding author(s). E-mail(s): francesca.basile@onera.fr;
Contributing authors: jean-baptiste.chapelier@onera.fr;
romain.laraufie@airbus.com; pascal.frey@sorbonne-universite.fr;

Abstract

In this paper, an *hp*-adaptation strategy designed for discontinuous Galerkin methods is extended and applied to hybrid RANS/LES simulations. The 3D *hp*-adaptive strategy is suited for tetrahedral and hybrid prismatic/tetrahedral meshes, and relies on a metric-based remeshing approach. The metric field and the polynomial map of the adapted meshes are built from an *a posteriori* error estimator which couples the measure of the energy associated with the highest-order modes and the inter-element jumps of the solution, combined with a smoothness sensor which guides the choice between *h*- and *p*-adaptation. The turbulence modeling relies on a Zonal Detached Eddy Simulation approach. The developed *hp*-adaptation algorithm is assessed in the context of hybrid RANS/LES simulations of the PPRIME nozzle configuration at diameter-based Reynolds number equal to $\mathbf{10^6}$, starting the adaptive process from previously RANS-adapted meshes. Far-field acoustic analysis are performed using a Ffowcs Williams-Hawkings method.

1 Introduction

In the design of novel engine nozzles concepts, scale-resolving simulations are of great interest in order to improve the understanding of turbulence and the noise generation mechanisms. Despite their extensive and well-assessed use for industrial configurations, Reynolds-averaged Navier-Stokes (RANS) simulations fail in predicting accurately non-equilibrium turbulent flows in which the turbulent large scales strongly affect the mean flow quantities [1], as for example with strongly detached and transitional flows [2]. RANS involves the solution of fluid dynamics equations considering time averaged quantities, such that the effects of the scales of turbulence are modeled. Large Eddy Simulation (LES) is designed to characterize explicitly the spatial and temporal dynamics of turbulent scales and the unsteady features encountered in transitional flows, gas turbine combustors, nozzles. Nonetheless, LES yields prohibitive costs to capture the wall-bounded turbulent dynamics at high Reynolds numbers. Hybrid RANS/LES models aim at combining the most attractive properties of the two approaches: the attached boundary layer is predicted by RANS models, while the unsteady 3D large eddies are captured by LES, decreasing the computational cost of separated turbulent flows with respect to LES. This allows for a strong reduction of the degrees of freedom (dofs) which wall-resolved LES would need to capture the smaller structures developed in the boundary layer.

Among the first hybrid RANS/LES methods introduced in the literature, the original Detached Eddy Simulation (DES) technique [3] is a non zonal approach with an automatic switch from RANS in the boundary layers to LES off walls driven by a sensor based on the mesh elements size. If the mesh is an "ambiguous mesh" not compliant with the DES requirements, the switch between the two models can be located in the boundary layer, resulting in an early switch to LES. As a consequence, the velocity fluctuations from the LES field do not balance the loss of the modeled Reynolds stresses. Spalart et al. [4] presented an improvement of the original DES, called Delayed DES (DDES), which detects the boundary layer with a sensor including information on gradients and viscosity. Among alternative approaches, the Zonal Detached Eddy Simulation (ZDES) framework aims at clearly separating the RANS and DES/DDES regions which are then linked through the definition of a hybrid length scale in the RANS equations [5]. The so-called ZDES mode 1 and 3 involve the user to define manually the RANS and DES regions, while the so-called mode 2 requires less input from the user and relies on shielding functions that automatically detect the regions to be treated with RANS or DES.

The simulation of turbulent unsteady phenomena requires as well accurate enough numerical schemes, presenting low dissipation and dispersion properties, for which discontinuous Galerkin (DG) methods [6, 7] are good candidates. These methods are based on the variational formulation of the governing equations and combine features of Finite Volume (FV) and Finite Element (FE) methods. Many aspects make DG methods particularly attractive, such as the high-order of accuracy achieved on arbitrary unstructured meshes, the accurate description of curved boundaries, the suitability to parallel computing

thanks to a compact stencil, and the possibility to exploit *a posteriori* jump and spectral error indicators for mesh adaptation. These error indicators are convenient thanks to their efficiency, locality, simplicity and low computational cost [8–11].

In particular the growing interest around DG lays in their *hp*-adaptivity, which means that one can not only locally adapt the size h of the mesh, but also the degree of the polynomials, p, within the element. In practice *hp*-adaptive methods lead to the concentration of the degrees of freedom in regions of interest of the flow, in order to optimize both the computational cost and the accuracy of the simulations [12–14].

Regarding *hp*-adaptivity, the local error estimator indicates the elements that should be refined, but does not inform whether to refine the element by h or p. A method for making this choice is called an *hp*-decision strategy. Generally this choice is made according to an estimate of the solution smoothness in an element: if it is sufficiently smooth, the adaptive algorithm opts for p-enrichment, while non-smooth zones are h-refined. Several strategies have been proposed concerning the *hp*-decision [8, 13–16]. In particular Mavriplis [8] determined if the solution is locally smooth or non-smooth by computing the decay rate of the Legendre expansion coefficients of the solution under the assumption that for non-smooth solutions, the discontinuities in the solutions deteriorate this decay rate.

The goal of the present work is to assess and apply an *hp*-adaptation algorithm to an unsteady flow configuration relevant in an industrial context, the subsonic isothermal jet issued from a round nozzle at $M_j = 0.9$ and $Re_D = 10^6$, with a hybrid RANS-LES approach, namely the ZDES combining modes 0 and 1. This formulation was proposed by Deck [17] in the framework of flows with separation fixed by the geometry, for which the boundary layer upstream the separation is forced to be solved with the RANS equations, while the separated zone is solved with DES equations. This approach has already been successfully applied to a wide range of cases [17, 18], including jet simulations [19–21]. In our work, the turbulent flow inside the nozzle is solved with RANS equations (mode 0 of ZDES), while the external jet region is solved with modified DES equations (mode 1 of ZDES).

An isotropic mesh refinement strategy is chosen to treat the free shear regions for which the small-scale structures present an isotropic character [22]. While turbulent scales can display an anisotropic behavior, the relative isotropy encountered at the scales located in the inertial range makes the isotropic remeshing approach viable for LES, although future research could tackle the anisotropy of turbulent structures as well. In the literature we can find examples of isotropic remeshing strategies, mostly for unsteady complex applications [23, 24].

In the context of LES/ILES simulations, pure p-adaptation has been successfully applied to DG methods [25–28] and is more popular than h-adaptation, which is usually preferred for FV and FE methods [23, 24, 29–32].

However, pure p-adaptation on fixed meshes needs the use of very high polynomial degrees to obtain a reasonable repartition of the degrees of freedom in the computational domain. Strong p variations can be cumbersome to optimize in terms of load balancing, while very high orders are associated with a more important cost per dof and can lead to numerical instabilities due to aliasing errors or very low levels of numerical dissipation/stabilization. Hence the interest of employing an hp-technique for DG schemes applied to LES, where the use of very high order polynomials is replaced by the possibility to adapt also the size of the elements. Static unsteady p-adaptation was performed by Chapelier et al. [25], de la Llave et al. [26] and Bassi et al. [27], while Abbà et al. [28] followed a dynamic approach.

As regards the h-adaptive side of our algorithm, a metric-based remeshing approach [33, 34] has been chosen for this work, showing promising results in the literature thanks to its flexibility to prescribe a precise size (and anisotropic features as aspect ratio and orientation in an anisotropic context) to each element of the mesh. The employed remeshing tool is MMG [35], which relies on primitive operators like edge splitting, edge collapsing, edge swapping, and node relocation, and has been already used extensively in the context of FV and FE methods [23, 24, 36, 37].

Concerning the estimation of the smoothness of the solution in each element, in this work we employ a slightly different formulation of the power decay of the modes from that proposed by Mavriplis and used in our previous work [38], which is found more appropriate in the context of scale-resolving turbulent flows [39]. The threshold value between smooth and non-smooth behavior is chosen as the theoretical value of the slope of the turbulent spectrum -5/3.

The anisotropy of the wall-attached flow inside the nozzle is treated with a fixed pseudo-structured layer of prisms, whose resolution can be modulated using a pure p-adaptive approach. The use of prismatic or hexahedral elements for the boundary layer region is in fact beneficial for computing the gradients with high-accuracy, in particular for RANS and hybrid RANS/LES simulations, where the near wall resolution constraint $y^+ \simeq 1$ is fundamental to obtain a relevant solution. To this end it is common that unstructured meshes involve a structured (extruded regular quadrilaterals) or pseudo-structured (extruded unstructured quadrilaterals or triangles) boundary layer around the body, which blends with the outer tetrahedral field regions [40–42]. In particular, in the field of nozzle/jet configurations an unstructured mesh approach has been extensively used in the literature, both for RANS simulations [43, 44] and LES of resolved jets [45, 46].

In the present work, the initial hp-mesh for starting the hybrid RANS/LES adaptation process is obtained via a series of low computational cost RANS hp-adaptations. The initial mesh can therefore capture some important features of the unsteady turbulent flow, which saves computational time, especially at the beginning of the adaptive procedure. This approach yields a robust and reasonably affordable means to achieve highly accurate hybrid RANS/LES simulations.

An *a posteriori* error estimator which employs the solution itself to derive estimates of the discretization error, is used to control the size of the elements of the mesh and the degree of their polynomial approximation. The error estimator couples two indicators, one based on the measure of the energy contained in the highest-order modes of the modal expansion and the other on the element interface momentum jumps. The coupling of these sensors guarantees a reasonable behavior both for high- and low-degree polynomial approximations. We also note that the part of the error estimator which is based on high-order modal energy bears a physical meaning relevant in the context of turbulent flows, as it is representative of the turbulent energy at the discretization cut-off wavenumber. This information is associated to the subgrid-scale activity and has been used to define the amplitude of eddy-viscosity based models [47, 48]. The error estimator is combined with a smoothness sensor which drives the *hp*-choice. The prescribed sizes are provided to the MMG remeshing library as an input size map, which outputs the newly adapted mesh. The solution on the previous mesh is projected on the newly adapted mesh, as well as the new prescribed polynomial degree map.

An acoustic post-processing is performed on the *hp*-adapted meshes of the PPRIME nozzle. The chosen hybrid approach for aeroacoustic predictions consists of solving the CFD field with scale-resolving simulations (DNS, LES, ILES, hybrid RANS/LES) to determine the near-field flow results, and then using these data to compute the far-field noise radiated from the jet using the Ffowcs Williams-Hawkings (FW-H) surface integral formulation [49]. This hybrid approach has been employed for jet noise predictions of different configurations, such as in installed wing/jet or isolated jets configurations [46, 50–58] as well as for other aircraft components as landing gears, flaps, rotors [59–63].

Flow simulations and error estimation are performed with the unstructured compressible flow solver CODA, developed in partnership by Airbus, ONERA and DLR [64], which targets research and industrial aerodynamic problems. Acoustic simulations are performed with the acoustic solver KIM [56] developed at ONERA.

The paper is organized as follows. Section 2 presents the details of the discretization of the ZDES mode 0+1 equations using the discontinuous Galerkin method, Section 3 provides a description of the *hp*-adaptive procedure and the implemented *hp*-adaptation algorithm is applied to the flow issued from a subsonic isothermal nozzle in Section 4. Results on the flow field and on the far-field acoustics are presented and compared to the experiments and numerical references in the literature. Concluding remarks and directions for future research are discussed in Section 5.

2 Numerical discretization of the governing equations

2.1 DG Discretization

The DG discretization of the compressible Navier-Stokes equations used in this work is based on a modal approach [65] that relies on the use of a hierarchical and orthogonal polynomial basis for the Galerkin projection. In this work unsteady solutions are obtained by employing an explicit three-stages Runge-Kutta scheme. The DG method implemented in the CODA solver is briefly outlined below.

We start by defining a shape-regular partition of the domain Ω, into a tessellation $\mathcal{T}_K$ of N non-overlapping and non-empty simplicial elements K of characteristic size h. Let $\mathcal{V}_h^p = \{\phi_h \in L^2(\Omega) : \phi|_K \in \mathcal{P}^p(K), \forall K \in \mathcal{T}_K\}$ be the functional space formed by piece-wise polynomials of degree at most p, and $\Phi_K = \{\phi_K^1, ..., \phi_K^{N_p}\}$ a hierarchical and orthonormal basis of $\mathcal{P}^p(K)$, of dimension N_p, confined to K. A methodology developed by Bassi et al. [66] consists in defining a starting set of monomial basis functions in each (arbitrarily shaped) element and applying a modified Gram-Schmidt orthonormalization procedure. The resulting basis yields a diagonal mass matrix in each element of the discretization, simplifying the resolution of the variational formulation. Φ_K^p is a hierarchical basis if it is contained in higher-order basis, that is $\Phi_K^p \subset \Phi_K^{p+1}$. The solution in each element is thus expressed as

$$\mathbf{u}_h(\mathbf{x}, t) = \sum_{q=0}^{p_K} \sum_{l \in d_q} \phi_K^l(\mathbf{x}) \mathbf{u}_K^l(t), \forall \mathbf{x} \in K, \quad K \in \mathcal{T}_K, \forall t \geq 0 \tag{1}$$

where $d_0 = \{1\}$ and $d_q = \left\{ l \in 2...N_p(K) \mid \phi_K^l \in \mathcal{P}_K^q \setminus \mathcal{P}_K^{q-1} \right\}$ is the set of indices of the basis functions of total degree q. The polynomial coefficients $(\mathbf{u}_K^l)_{1 \leq l \leq N_p}$ represent the degrees of freedom of the discrete problem in element K.

The conservation law is discretized in physical space by using a discontinuous Galerkin method and the semi-discrete variational form of the system of Navier-Stokes equations thus reads: find $\mathbf{u}_h$ in $\mathcal{V}_h^p$ such that $\forall \phi_h \in \mathcal{V}_h^p$ we have

$$\int_{\mathcal{T}_K} \phi_h \partial_t \mathbf{u}_h dV + \boldsymbol{\mathcal{L}}_c(\mathbf{u}_h, \phi_h) + \boldsymbol{\mathcal{L}}_v(\mathbf{u}_h, \boldsymbol{\sigma}_h, \phi_h) = 0 \, . \tag{2}$$

In equation (2) $\boldsymbol{\mathcal{L}}_c$ and $\boldsymbol{\mathcal{L}}_v$ represent the weak form of the convective and viscous terms respectively.

The following notations are introduced: for a given interface e in $\mathcal{E}_i$ we define the average operator as $\{\{\mathbf{u}\}\} = (\mathbf{u}^+ + \mathbf{u}^-)/2$, the jump operator is defined as $[\![\mathbf{u}]\!] = \mathbf{u}^+ \otimes \mathbf{n} - \mathbf{u}^- \otimes \mathbf{n}$ where $\mathbf{u}^+$ and $\mathbf{u}^-$ are the traces of the variable $\mathbf{u}$ at the interface between elements K^+ and K^-. The DG discretization of

the convective terms then reads:

$$\begin{aligned}\boldsymbol{\mathcal{L}}_c(\mathbf{u}_h, \phi_h) = &- \int_{\mathcal{T}_K} \mathbf{F}_c(\mathbf{u}_h) \cdot \nabla_h \phi_h dV + \int_{\mathcal{E}_i} [\![\phi_h]\!] \mathbf{h}_c(\mathbf{u}_h^+, \mathbf{u}_h^-, \mathbf{n}) dS \\ &+ \int_{\mathcal{E}_b} \phi_h^+ \mathbf{F}_c(\mathbf{u}_b) \cdot \mathbf{n} dS \,,\end{aligned} \tag{3}$$

where the boundary values $\mathbf{u}_b = \mathbf{u}_b(\mathbf{u}_h^+, \mathbf{u}_{ext}, \mathbf{n})$, with $\mathbf{u}_{ext}$ a reference external state computed such that the boundary conditions are satisfied on $\mathcal{E}_b$. The numerical flux $\mathbf{h}_c$ is chosen such that it is consistent and conservative.

The discretization of the convective terms in this work is performed by using the Roe flux [67] with an entropy fix similar to that of Harten [68].

The discretization of the viscous terms is performed using the BR1 approach of Bassi & Rebay [69]. This approach relies on the definition of the conservative variable gradients as auxiliary variables $\boldsymbol{\sigma}_h = \nabla_h \mathbf{u}_h + \mathbf{L}_h$. This leads to the introduction of the so called global lifting operator $\mathbf{L}_h$, which depends on the inter-element jumps of the solution [69].

The discrete variational form of the viscous term for the BR1 method therefore reads:

$$\begin{aligned}\boldsymbol{\mathcal{L}}_v(\mathbf{u}_h, \boldsymbol{\sigma}_h, \phi_h) = &\int_{\mathcal{T}_K} \mathbf{F}_v(\mathbf{u}_h, \nabla_h \mathbf{u}_h + \mathbf{L}_h) \cdot \nabla_h \phi_h dV \\ &- \int_{\mathcal{E}_i} [\![\phi_h]\!] \{\{\mathbf{F}_v(\mathbf{u}_h, \nabla_h \mathbf{u}_h + \mathbf{L}_h)\}\} \cdot \mathbf{n} dS \\ &- \int_{\mathcal{E}_b} \phi_h^+ \mathbf{F}_v(\mathbf{u}_b, \nabla_h \mathbf{u}_b + \mathbf{L}_h) \cdot \mathbf{n} dS \,.\end{aligned} \tag{4}$$

The integrals in the above formulas are computed by numerical integration, with specific quadrature rules depending on the type of element/face being considered. Quadrilateral and hexahedral elements use tensor-product formulas obtained from the 1D Gauss-Legendre quadrature rule. Numerical integration on triangles and tetrahedra is efficiently performed by means of the optimized quadrature rules proposed by Witherden et al. [70]. Prismatic elements employ a combination of a Gauss-Legendre quadrature in the extrusion direction and the aforementioned optimized quadrature for triangles in the other two directions.

2.2 The Zonal Detached Eddy Simulation Mode 0+1

The Zonal Detached Eddy Simulation (ZDES) which is used in this work is a hybrid RANS/LES technique, formalized by Deck [17] and initially based on the Spalart Allmaras (SA) [71, 72] RANS model, as an efficient solution to achieve a faster decay of the eddy viscosity in the LES mode with respect to classical DES/DDES.

In the ZDES framework, the wall distance d_w of the SA turbulent variable transport equation, is replaced with the hybrid length-scale $\tilde{d}_{ZDES}$. In practice

this modification is active in the destruction term of the RANS-SA equation. Using the formulation known as the "negative" version of the SA model, the eddy viscosity is defined as:

$$\mu_t = \begin{cases} \rho\tilde{\nu} f_{v1} & \text{for } \tilde{\nu} \geq 0 \\ 0 & \text{for } \tilde{\nu} < 0 \end{cases} \tag{5}$$

with f_{v1} a near-wall correction function [71].

The eddy viscosity in the LES region scales then with the length-scale and the vorticity magnitude $\rho\tilde{\nu} \sim \tilde{\omega}\tilde{d}^2_{ZDES}$. The first version of ZDES chosen in this work is generally employed for flow configurations where the position of the separation is known a priori from the geometry, namely for massively separated flows. In particular a user-defined zonal decomposition of the computational domain in RANS and DES areas allows for the fully attached boundary layer regions to be solved with RANS equations. This prevents the so-called "grid-induced separation" phenomenon [4] which can appear when a mesh is too fine in the longitudinal direction, where the original DES approach would reduce the RANS viscosity.

In the current work, where the studied test case is a jet issued from a nozzle, the model will be set to RANS mode (mode 0 of ZDES) inside the nozzle, as depicted in figure 1.

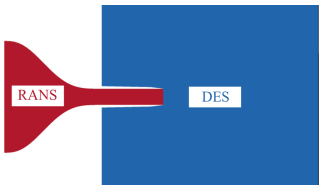

Fig. 1: hpDG/ZDES simulations of the PPRIME nozzle. Forcing of the interior of the nozzle to RANS mode.

The hybrid length in the destruction term of the SA equation is defined as:

$$\tilde{d}_{ZDES} = \begin{cases} d_w & \text{in RANS zones} \\ \min(d_w, C_{DES}\tilde{\Delta}_{DES}) & \text{in DES zones} \end{cases} \tag{6}$$

where C_{DES} is a coefficient usually set to 0.65 which has been calibrated from decaying homogeneous turbulence simulations [73].

Three aspects differentiate this formulation from the classical DES [3]. The first is that the sub-grid length scale $\tilde{\Delta}_{DES}$ is defined using the cubic root of the volume of the cell $\Delta_{vol} = \sqrt[3]{|K|}$, where $|K|$ is the volume of the element K, and not the maximum grid extension $\Delta_{max} = \max(\Delta_x, \Delta_y, \Delta_z)$. Moreover this length scale is divided by the number of 1D degrees of freedom for a DG method, similarly to Lorteau et al. [46] who considered this definition for

performing LES of jet flows using tetrahedral meshes, in order to obtain the high-order sub-grid length scale of the DES model $\tilde{\Delta}_{DES} = \frac{\Delta_{vol}}{p+1}$ [74]. The last change consists in the modification of the near-wall correction functions f_{v1}, f_{v2} and f_w of the SA-RANS model. In the original formulation for RANS equations, f_{v1} and f_{v2} are defined to ensure that $\tilde{\nu} = \kappa u_\tau y$ in the viscous layer, the log-layer and in the buffer layer, and that $\tilde{S} = u_\tau / \kappa d_w$ in the log-layer, where u_τ is the friction velocity, $\tilde{S}$ the modified vorticity in the production term of the SA model and $\kappa = 0.41$ the von Kármán constant. The function f_w is a correction used to reduce the turbulent viscosity in the outer region of the boundary layer.

In the current work the near-wall corrections are the same as the RANS Spalart-Allmaras model in RANS mode, while in LES mode they are modified as suggested in [5]:

$$f_{v1} = 1 \,, \qquad f_{v2} = 0 \,, \qquad f_w = 1 \,, \tag{7}$$

which are their asymptotic values far from the wall, avoiding a drop of subgrid viscosity that could be caused by the damping functions of the RANS model in resolved LES zones presenting low eddy viscosity levels. The reader is referred to [5, 71, 72] for further implementation details and discussion of the RANS-SA model and its modifications proposed for scale-resolving simulations.

3 The *hp*-adaptive algorithm

The *hp*-strategy proposed in the present paper for hybrid RANS/LES simulations derives from a previous work which focused on steady laminar and RANS simulations. A comprehensive description of the method is available in [38], while we focus here on the description of the extension of the method to the unsteady hybrid RANS/LES formalism. The main ingredients of the original *hp*-methodology are reminded briefly as well.

Accurate DG-based *a posteriori* indicators extracted from the DG flow solver CODA are coupled with the remeshing library MMG. This error estimator identifies the regions lacking accuracy, improving their resolution by either decreasing the size of the element or increasing the polynomial degree which approximates the solution. A smoothness indicator guides the *hp*-decision, leading to *p*-enrichment for smooth regions and *h*-refinement for non-smooth regions.

The *hp*-adaptive algorithm, initially based on fully simplicial meshes (triangles in 2D and tetrahedra in 3D) and then extended to hybrid-meshes, permits to take into account elements which cannot be remeshed. A variable polynomial degree setting adapts the resolution of the fixed elements by increasing their polynomial degree, overcoming the constraint that elements with a fixed geometry impose in a pure *h*-adaptive context. In these regions the *hp*-choice is relaxed, and an element requiring increased resolution does not need anymore to be smooth to be *p*-adapted: a value of the error estimator greater than the target error estimator is sufficient to mark it for *p*-refinement.

The adaptation strategy can be applied similarly for static *h/hp*-adaptation of unsteady flows. In this case the adaptive algorithm is applied once a pseudo-steady state of the flow is reached. Instead of the instantaneous values, the time-average of the error estimator accumulated for a given period is considered.

3.1 Error estimator

We use here an accurate and simple error estimator suited for various polynomial degrees. In previous work [38], we followed the same idea of Colombo et al. [75] and Bassi et al. [27] by combining two error estimators. One is based on the energy of the highest-order modes, the Small Scale Energy Density (SSED) ϵ_{SSED} [76], while the other is based on the jumps across element interfaces, ϵ_{JUMP} [77]. The reasons of this choice lie in the fact that an error indicator based on the highest order modes of the solution is only reliable for a high p, while a jump-based error estimator is accurate for every polynomial degree. The formulation of the error estimator presented in [38], and used in the present work, is here recalled.

The SSED error estimator is based on a measure of the discretization error of the numerical solution $\mathbf{u}$ by computing the norm of the difference between the numerical solution $\mathbf{u}_{h,p}$ and the projection of the numerical solution on the reduced-order space $\mathcal{V}_h^{p-1}$, namely $\mathbf{u}_{h,p-1}$:

$$\epsilon^2_{\text{SSED},K} = \frac{\int_K ||(\rho\mathbf{v})_{h,p} - (\rho\mathbf{v})_{h,p-1}||^2 dV}{|K|} = \frac{||(\rho\mathbf{v})_{h,p} - (\rho\mathbf{v})_{h,p-1}||^2_{L^2(K)}}{|K|} \quad (8)$$

The estimator is divided by the volume of the element K. $(\rho\mathbf{v})_h$ represents the momentum vector.

The second error estimator is based on the assumption that, at a given interface e of an element K (an edge in 2D, a face in 3D), the error on the interface e can be defined as half the jump of the variable traces across the interfaces.

Therefore we can build an averaged error estimator over each interface e, for the norm of the momentum vector, and normalize it by the area of each interface $|\partial K_e|$ for consistency with the dimensions of the SSED indicator in equation (8). Finally, the error estimator on the element K is an average of an estimator computed on each interface e of the element K:

$$\epsilon^2_{\text{JUMP},K} = \frac{1}{N_e}\sum_{e=1}^{N_e} \frac{\int_{\partial K_e} ||(\rho\mathbf{v})_h^+ - (\rho\mathbf{v})_h^-||^2 dS}{4|\partial K_e|} = \frac{1}{N_e}\sum_{e=1}^{N_e} \frac{||(\rho\mathbf{v})_h^+ - (\rho\mathbf{v})_h^-||^2_{L^2(\partial K_e)}}{4|\partial K_e|} \quad (9)$$

where N_e the number of faces of the element in 3D (or edges in 2D).

Both indicators are normalized by their respective maximum and minimum values over the whole domain $\mathcal{T}_K$ (min-max normalization) before the coupling:

$$\begin{aligned}\epsilon_K &= \epsilon_{\text{SSED},K,norm} + \epsilon_{\text{JUMP},K,norm} \\ &= \frac{\epsilon_{\text{SSED},K} - \min(\epsilon_{\text{SSED}})_{\mathcal{T}_K}}{\max(\epsilon_{\text{SSED}})_{\mathcal{T}_K} - \min(\epsilon_{\text{SSED}})_{\mathcal{T}_K}} + \frac{\epsilon_{\text{JUMP},K} - \min(\epsilon_{\text{JUMP}})_{\mathcal{T}_K}}{\max(\epsilon_{\text{JUMP}})_{\mathcal{T}_K} - \min(\epsilon_{\text{JUMP}})_{\mathcal{T}_K}}\end{aligned} \tag{10}$$

3.2 Smoothness indicator

A crucial point in *hp*-adaptive methods lies in the definition of a relevant strategy to choose whether to adapt an element with *h*-refinement or *p*-enrichment. In our previous work [38], we adopted the approach initially proposed for 1D by Mavriplis in [8], which follows the assumption that the decay rate of the spectrum of DG modal coefficients is related to the convergence rate of the solution. This information is exploited to evaluate the smoothness of the solution in the elements in the mesh. In the present work, we propose an alternative definition of the smoothness indicator that is taking into account the underlying physics of unsteady turbulent flows. It is assumed that for a 1D Legendre expansion of coefficients $q = 0, ..., p_K$ the power decay of the modes q can be expressed as:

$$E^{(q)} \simeq Cq^{-\sigma} \tag{11}$$

where $E^{(q)}$ is the energy associated with the mode q, C and σ are constants determined by a least-squares best fit of $\log(E^{(q)})$ vs. $\log(q)$. The decay coefficient σ is then used as smoothness indicator. In particular, the modal energy is proportional to the square of the momentum $E^{(q)} \propto \left(a^{(q)}\right)^2$, where $a^{(q)}$ are the polynomial coefficients associated with the norm of the momentum for the q-th mode. High decay rates imply that the solution is smooth, while the solution deviates from analytical behavior in presence of low decay rates. This particular formulation of the decay rate is interesting for turbulent flows as it corresponds to the slope of spectral decay for the energy carried by turbulent scales. We can therefore draw a similarity with the classical Fourier analysis of turbulence and in particular the universality of the energy decay slope in the inertial range. Although the spectrum is built using a limited sampling determined by the size of the polynomial basis, the range of scales covered by the polynomial modes considered is likely to represent scales located in the inertial range. Indeed, DG discretizations feature two distinct spectral cut-off wavenumbers, the first associated to the mesh, and the second associated to the full discretization including the polynomial expansion. The evaluated spectrum inside each mesh element is therefore representative of the range of scales between these two cut-offs.

In the context of the calibration of a spectral dynamic modeling procedure for Large Eddy Simulation, Chapelier et al. [39] observed that high values of σ are found in laminar or well-resolved regions, while low values are likely to appear in elements presenting an intense but poorly resolved small-scale activity. They used this evaluation of the energy decay as an estimation of the

quality of the resolution in each element, allowing for adapting the intensity of the sub-grid dissipation locally. They evaluated *a priori* the threshold value of under-resolution σ_{thr} from Taylor-Green Vortex (TGV) Direct Numerical Simulation data at $Re = 5000$ and they obtained values very close to the theoretical slope -5/3 found in Fourier space in the inertial range. Therefore they were able to link the smoothness indicator to the universal $-5/3$ power law which uniquely describes the shape of the energy spectrum in the inertial subrange. This indicator driving the subgrid dissipation was found to behave consistently when considering irregular meshes, various polynomial degrees and flow cases [78]. We can exploit the same observations and use the value $\sigma_{thr} = 5/3$ as the threshold between smooth and non-smooth behavior in our work. Elements with $\sigma_K > 5/3$ are assumed to be smooth, and subject to p-enrichment; if this condition is not fulfilled h-refinement is used to solve locally the problem of under-resolution associated with unphysical spectral decay.

Since for 2D and 3D computations, several modal coefficients can contribute to the energy at index q, we need to gather the coefficients of the modes to retrieve one single value per index q. The approach we follow in our work consists in computing the coefficient $a^{(q)}$ as the L^2-norm of $u^{(q)}$ of the coefficients of the polynomial basis as:

$$a_K^{(q)} = \sqrt{\sum_{l \in d_q} u_K^{(l)^2}} \quad \forall q \in (1, p_K) \, . \tag{12}$$

The coefficient associated to $q = 0$ represents the cell-averaged solution, and it can severely bias the decay rate. Therefore we chose not to employ the coefficient $a^{(0)}$ in the log-log regression $\log(a^{(q)})^2$ vs. $\log(q)$. This means that we can compute the smoothness indicator only for high-order elements $p \geq 2$. Therefore in this work we decided to always fictitiously mark $p = 1$ elements as smooth elements, always requiring p-adaptation.

Moreover we use the smoothness indicator also as indicator of the convergence rate of the solution, which will be explained in detail in the following sections.

3.3 Strategy for unsteady flows

The strategy is to first perform a series of *hp*-adaptations using affordable steady RANS simulations which in turn provide a starting mesh for the hybrid RANS/LES adaptation that already captures some important features of the unsteady simulation. This approach, where the accurate and expensive hybrid RANS/LES adaptation is performed starting from a RANS-adapted mesh, is preferred over starting the adaptation process on a very coarse mesh with hybrid RANS/LES simulations. Such a mesh would prevent the turbulent structures of the flow from developing, and could yield numerical instabilities and very poor quality results. Moreover it would dramatically increase the computational time for the whole adaptation process, as many unsteady adaptation steps would be needed to reach accurate results.

Starting from a RANS solution is also natural in the present hybrid RANS/LES context, as the wall-attached flow (and eventually other critical zones using a zonal DES approach) is solved in RANS mode, and a ZDES statistically-steady flow can be easily established from a RANS solution, after passing a transient period T_{trans}.

Once a statistically-steady solution has been reached, the error estimator is accumulated for a relatively short time period $T_{\epsilon\sigma}$, with respect to the total simulation time needed for data analysis and statistics collection T_{stats}. This allows the user to perform the successive adaptation steps without accumulating flow statistics for a long time. In fact the error estimator is very sensitive to poorly-resolved zones, and does not need a very long time to become representative in such zones needing an improved resolution. Both the error estimator/smoothness indicator and the flow data are sampled at a constant sampling time step Δt_{sampl}.

After each adaptation and projection of the previous solution on the newly adapted mesh, the error and the smoothness estimator and flow data statistics are collected after a transient T_{trans}. This transient is necessary in order to let the solution adapt to the new mesh.

The transient period T_{trans}, the collection period of the error estimator and the smoothness indicator $T_{\epsilon\sigma}$, and the sampling time interval Δt_{sampl} are generally case-dependent, as well as the total simulation duration where flow statistics are collected T_{stats}. Thus they must be chosen accordingly to features depending on the studied flow.

3.4 Degree and metric prescription

The method consists in performing successive simulations, with a mesh and polynomial degree refinement at each step. The methodology used in the present work is suited for hybrid meshes: during the adaptation process, boundary layer structured or pseudo-structured elements are kept unchanged, and the remeshing adaptive algorithm acts only for tetrahedra. No specific development is made to the MMG library, which preserves prisms (quadrilaterals in 2D) by default.

For hybrid meshes the elements are split into two parts:

$$\mathcal{T}_{K,i} = \mathcal{T}_{\text{free},i} \cup \mathcal{T}_{\text{fixed},i} \ , \tag{13}$$

where $\mathcal{T}_{\text{free},i}$ is the tetrahedral zone subject to remeshing, and $\mathcal{T}_{\text{fixed},i}$ includes the prismatic layer and the internal tetrahedra, which are considered only for p refinement.

We define as well three non overlapping sets of mesh elements:

$$\mathcal{T}_{K,i} = \mathcal{T}_{h,i} \cup \mathcal{T}_{p,i} \cup \mathcal{T}_{=,i} \ , \tag{14}$$

where $\mathcal{T}_{h,i}$ is the subset of the elements marked for h-adaptation, $\mathcal{T}_{p,i} = \mathcal{T}_{p,\text{free},i} \cup \mathcal{T}_{p,\text{fixed},i}$ is the subset of the elements marked for p-adaptation, which

can include tetrahedral elements or fixed prismatic elements, and $\mathcal{T}_{=,i}$ is the subset of the elements not marked for any adaptation. An element cannot be selected for both h- and p-adaptation.

We summarize here the steps to perform the adaptive procedure starting from a RANS-adapted mesh $\mathcal{T}_{K,0}$, for which the variable degree distribution p_0 and the characteristic lengths field h_0 are available. We recall that the index i identifies the step of the adaptive procedure.

1. A DG computation is performed to establish a statistically-steady state solution on $\mathcal{T}_{K,i}$ for a period T_{trans}.
2. The *a posteriori* error estimator $\epsilon_{K,i}$ is computed on each element of $\mathcal{T}_{K,i}$ from the DG solution and averaged for a period $T_{\epsilon\sigma}$.
3. The smoothness indicator $\sigma_{K,i}$ is computed on each element of $\mathcal{T}_{K,i}$ from the DG solution and averaged for a period $T_{\epsilon\sigma}$.
4. The target error map ϵ^*_{i+1} is determined from the error estimation $\epsilon_{K,i}$ and the desired number of degrees of freedom following an iterative procedure described below.
5. Elements with poor resolution, and presenting fixed geometry or a $p1 =$ discretization, are marked for p-enrichment:

$$\mathcal{T}_{p,\text{fixed},i} = \{K \in \mathcal{T}_{\text{fixed},i} \mid \epsilon_{K,i} > \epsilon^*_{K,i+1} \text{ and } p_{K,i} + 1 \leq p_{\max}\} \tag{15}$$

6. Elements with poor resolution, and free to be h- or p-adapted, are marked for p-enrichment:

$$\begin{aligned}\mathcal{T}_{p,\text{free},i} = \{&K \in \mathcal{T}_{\text{free},i} \mid \epsilon_{K,i} > \epsilon^*_{K,i+1} \text{ and} \\ &[(\sigma_{K,i} > 5/3 \text{ and } p_{K,i} + 1 \leq p_{\max}) \text{ or } p_{K,i} = 1]\}\end{aligned} \tag{16}$$

7. Elements with poor resolution, and free to be h- or p- adapted are marked for h-adaptation:

$$\begin{aligned}\mathcal{T}_{h,\text{free},i} = \{&K \in \mathcal{T}_{\text{free},i} \mid \epsilon_{K,i} > \epsilon^*_{K,i+1} \text{ and} \\ &[\sigma_{K,i} \leq 5/3 \text{ or } (\sigma_{K,i} > 5/3 \text{ and } p_{K,i} + 1 > p_{\max})] \text{ and } p_{K,i} \neq 1\}\end{aligned} \tag{17}$$

8. The polynomial degree of elements marked for p-adaptation is defined as:

$$p^*_{K,i+1} = \max(p_{K,i} + 1, p_{max}), \qquad \forall K \in \mathcal{T}_{p,i} \tag{18}$$

9. The size of elements marked for h-adaptation is adapted. The input size-field that MMG requires is node-based, however our error estimator, smoothness indicator and polynomial degree are element-based. Therefore a volume-weighted average is applied to these quantities. In particular, they are only computed from the elements surrounding the node n which have not been marked for p-enrichment at the current step.

   - The polynomial degree $p_{K,i}$ is averaged to the nodes $p_{n,i}$.

- The error estimator $\epsilon_{K,i}$ is averaged to the nodes $\epsilon_{n,i}$.
- The smoothness indicator $\sigma_{K,i}$ is averaged to the nodes $\sigma_{n,i}$.
- The size h_n^* is imposed at the node n:

$$h^*_{n,i+1} = h_{n,i} \left(\frac{\epsilon^*_{i+1}}{\epsilon_{n,i}} \right)^{\frac{1}{m_{n,i}}} \qquad \forall n \in \mathcal{T}_{h,free,i} \tag{19}$$

- A convergence rate $m_n = p_n + 1$ is imposed if the solution is smooth ($\sigma_n > 5/3$), and $m_n = 1$ if the solution is non-smooth ($\sigma_n \leq 5/3$).
- A user-defined factor, the maximum refinement factor r_h, is necessary to avoid uncontrolled size changes between two consecutive adaptation steps. In one adaptation step the edge can decrease its size by at most r_h times, i.e. $h^*_{n,i+1} \geq h_{n,i}/r_h$.

10. The new metric is given to MMG, which generates the refined mesh $\mathcal{T}_{K,i+1}$.
11. The new polynomial degree map $p^*_{K,i+1}$ is projected from $\mathcal{T}_{K,i}$ to $\mathcal{T}_{K,i+1}$ thanks to a nearest neighbor interpolation.
12. The solution of $\mathcal{T}_{K,i}$ is projected on the newly adapted mesh $\mathcal{T}_{K,i+1}$ with an L^2 projection.

We perform these steps until we reach a certain threshold, which in our case is the maximum number of dofs we want to compute.

Adopting this strategy, the regions presenting a higher error estimator value than the target, with smooth solution, $p = 1$ approximation, or fixed elements, are p-enriched, while the regions with non-smooth solution (or already at their maximum polynomial degree $p_{\max}$, where h-adaptation is enforced) are refined of a factor depending on the ratio between the target error and the value of the error estimator.

The target error ϵ^*_{i+1}, common to all nodes is chosen with an iterative procedure, such that the number of degrees of freedom is increased at each adaptation step by a fixed percentage f_r. Let N_{i+1} be the number of dofs in the i-th mesh, and N^*_{i+1} be the number of dofs in the new *(i+1)*-th mesh, the desired number of dofs for the new mesh *(i+1)*-th is defined as $\mathrm{N}^*_{i+1} = f_r \cdot \mathrm{N}_i$ dofs.

Note that coarsening is not integrated in the present approach. Instead, we rely on defining very coarse initial meshes, such that the regions of interest will be progressively refined following each adaptation step, while the regions of the flow characterized by low resolution requirements retain the coarse discretization properties of the initial mesh. This approach is suitable for the static adaptation and the statistically steady flows considered in the present study.

4 Application to the isothermal subsonic turbulent jet flow issued from the PPRIME nozzle at $Re_D = 10^6$

In this section, we apply the *hp*-methodology initially introduced in [38] and extended to unsteady flows in section 3, to ZDES computations of a nozzle configuration. The nozzle test case analyzed in this work corresponds to the configuration described in [79], for which experiments have been performed at the Bruit & Vent jet-noise facility of the Institut PPRIME, Poitiers, France, with available reference data. Numerical results are available as well in the literature: this configuration has been simulated with LES by Brès et al. [79] to analyse features such as near-wall adaptive mesh refinement, synthetic turbulence and wall modeling inside the nozzle in LES, with hybrid RANS/LES by Gand & Huet in [80] to assess the generation of a turbulent inflow and with RANS by Neifeld et al. [81] for jet noise prediction purposes with eddy relaxation source model.

First, flow field results are presented, assessed and compared to those obtained by other authors in the literature.

In the second part of this section, an aeroacoustic analysis is performed in order to predict far-field noise, which is known to be a major issue in the conception of aircraft. A Ffowcs Williams-Hawkings method (FW-H) [49] is employed in this work for this purpose. In fact, the propagation of the noise generated from jets to the far-field, using only LES, has still a prohibitive computational cost. Hence the need of an integral method as the FW-H formulation, which has been widely employed for acoustic post-processing of jets simulations as well as other air-frame configurations [46, 50–63]. This method allows for computing the acoustic radiation of the acoustic sources generated by a turbulent flow: starting from the fluid flow field computed with LES on a surface enclosing the noise sources, the noise is propagated to the observer located far from the noise source.

4.1 Flow field computational set-up

The operating conditions are defined in terms of the total pressure ratio $\mathrm{p}_t/\mathrm{p}_\infty = 1.7$ and total temperature ratio $T_t/T_\infty = 1.15$. We refer to jet properties with the subscript j. The jet is isothermal ($T_j/T_\infty = 1.0$), the jet Mach number is $M_j = U_j/c_j = 0.9$, and the Reynolds number is $Re_D = \rho_j U_j D/\mu_j \simeq 1 \cdot 10^6$, where U_j is the mean jet exit longitudinal (x-direction) velocity, c is the speed of sound, ρ is the density, μ is the dynamic viscosity and $D = 0.05m$ is the diameter of the nozzle. The characteristic time scale is $t_c = D/U_j$. A slow coflow at Mach number $M_\infty = 0.01$ is imposed outside the nozzle (the flow is at rest in the experiment). Imposing a slow coflow was considered in previous numerical studies, namely [79] and [80], among others. In particular, in [79] the authors justify its use to prevent spurious recirculation and facilitate flow entrainment.

All solid surfaces of the nozzle are treated as no-slip adiabatic walls. Far-field boundary conditions are imposed on the lateral and inflow surfaces of the external cylindrical domain, the relevant stagnation pressure and temperature are defined at the inflow of the nozzle and the free-stream static pressure is specified at the outlet.

The axisymmetric computational domain extends from approximately $-10D$ (the longitudinal length of the nozzle in the x-direction) to $50D$ in the longitudinal direction x, and from $-30D$ to $30D$ in the radial direction. The full extent of the nozzle geometry is represented and its exit in the axis is located at $(x, y, z) = (0, 0, 0)$.

A prismatic boundary layer is extruded in the direction normal to the surface of the nozzle, and the rest of the domain is filled with tetrahedra. The prismatic boundary layer is kept fixed during the whole adaptation process, since pure metric-based mesh adaptation can handle only simplicial meshes (triangles in 2D and tetrahedra in 3D). These elements can only be p-adapted. The wall-normal spacing of these near-wall prisms is set such that we obtain an accurate representation of the turbulent boundary layer using the SA model with $p_{max} = 3$, following the guidelines of Basile et al. [82].

In addition to the prismatic boundary layer, it has been chosen to preserve also the tetrahedral elements internal to the nozzle. Tetrahedra free to change size inside the nozzle but constrained by the fixed prismatic surfaces can severely affect the quality of the mesh. This can be easily done thanks to the ability of MMG to preserve tetrahedra specified by the user. These elements will be subject to p-adaptation only.

The initial mesh *hp*G1 employed in this work is an *hp*-mesh obtained from a steady *hp*-adaptation using RANS equations to solve the nozzle/jet flow [38]. Three previous steps of RANS adaptation have been performed starting from a very coarse mesh counting 1.5 million dofs. The *hp*G1 mesh, counting 11.6 million dofs and attaining a sufficient level of convergence with RANS equations, is used as starting point for ZDES mesh adaptation. Two ZDES adaptation steps are performed, yielding a discretization *hp*G2 with 18.9 million dofs, and a discretization *hp*G3 with 31.7 million dofs.

A sponge layer is created for elements presenting their cell centers more than 35 diameters far from the nozzle exit in the streamwise direction $x_c > 35D$, and 10 diameters from the axis of the jet $r_c > 10D$ in the radial direction. The mesh elements in these regions have a very large size which can compromise the stability of the simulations when turbulent structures or high amplitude sound waves pass through them, if a high order of accuracy is defined in those cells. An elegant way fitting to the present *hp*-methodology consists in forcing these elements to a low order $p = 1$ discretization. This creates a sponge layer which further damps the aforementioned problematic phenomena as well as reducing the overall computational burden of the simulations. This forcing is kept active through the adaptive procedure (figure 2).

In the right panel of figure 2, the high-order pressure fluctuations field is projected on a fine mesh from an instantaneous DG solution of the *hp*G1

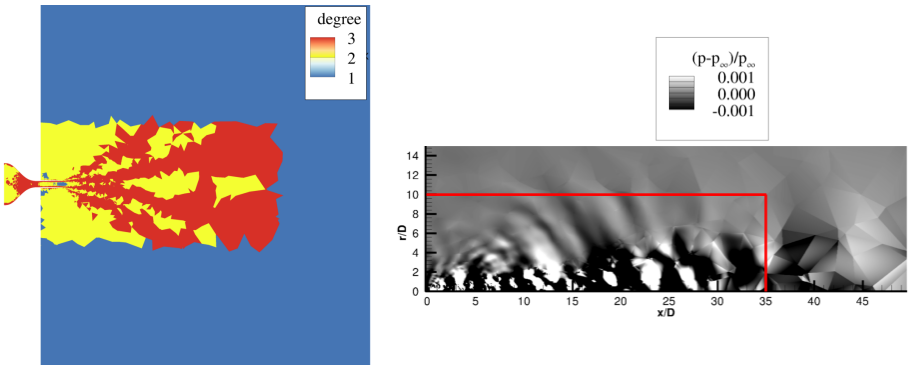

Fig. 2: hpDG/ZDES simulations of the PPRIME nozzle. Left: Slice of the computational domain for the *hp*G1 discretization with the polynomial degree map. Right: Instantaneous pressure fluctuations contours in grey scale, extracted from the high-order solution interpolated on a fine post-processing mesh, with the $p = 1$ sponge layer interface marked with a solid red line.

discretization. The acoustic field is briefly analyzed to assess potential acoustic reflections generated by the sponge layer zone (whose interface is marked by the red lines) or variations in the polynomial degree p. From a qualitative perspective, no significant reflections of spurious acoustic waves across the sponge layer interface are observed. The identification of acoustic sources due to p-interfaces in the jet would require a finer analysis, however, no major reflections seem to be affecting the acoustic field, which correctly propagates to the far-field with a preferred direction in the range between $\theta \sim 40°$ and $20°$ above the jet axis.

The time intervals required to pass the transient and collect the error estimator statistics, introduced in section 3.3, are chosen as follows:

- $T_{\text{trans}} = 50t_c$, the time required to evacuate the transient phenomena and the starting point of the collection of flow statistics.
- $\Delta t_{\text{sampl}} = 0.0067t_c$, which means 150 samplings for each t_c.
- $T_{\epsilon\sigma} = 30t_c$, the time window during which the smoothness indicator and error estimator are collected and averaged.
- $T_{\text{stats}} = 150t_c$, the time window during which the flow statistics are collected.

The parameters used by MMG and the adaptation module are:

- $h_{grad} = 1.5$, showing a good compromise between excessive refinement induced by a low value of h_{grad}, and the loss of isotropy and mesh quality induced by a high value. This parameter controls the ratio between the lengths of two adjacent edges.
- $h_{min,\text{tetra}}$ is set to $h_{min} = 0.016D$ for tetrahedra, which is the length of the smallest edge of the boundary layer prisms which constitutes the interface with tetrahedra. The height of the first element of the prismatic layer is

$h_{min,\text{prisms}} = 0.0003D$, and is fixed along the geometry and over the course of the adaptive procedure.

- h_{max} is set as the size of the domain where far-field boundary conditions are imposed.
- $r_h = 4$ such that between two steps of the adaptation process, the edge of the equilateral triangle can at most divide by four its size.
- $f_r = 2$ such that the desired number of dofs in the newly adapted mesh is twice the number of dofs present in the previous mesh. We remind that the adaptive procedure, together with the remeshing step performed by MMG, is not always able to respect the exact desired number of dofs, while however providing a good guess.
- $p_{\text{min}} = 1$ is the minimum polynomial degree of the spatial discretization allowed for *hp*-adaptation.
- $p_{\text{max}} = 3$ is the maximum polynomial degree that the spatial discretization is allowed to reach for *hp*-adaptation.

4.2 Flow field results

4.2.1 Computational meshes

Figure 3 shows the three *hp*-meshes employed in this study: *hp*G1, the initial *hp*-mesh of the ZDES adaptive procedure, adapted from a previous RANS adaptation; *hp*G2, the first adapted *hp*-mesh from a ZDES simulation; *hp*G3, the second adapted *hp*-mesh from a ZDES simulation.

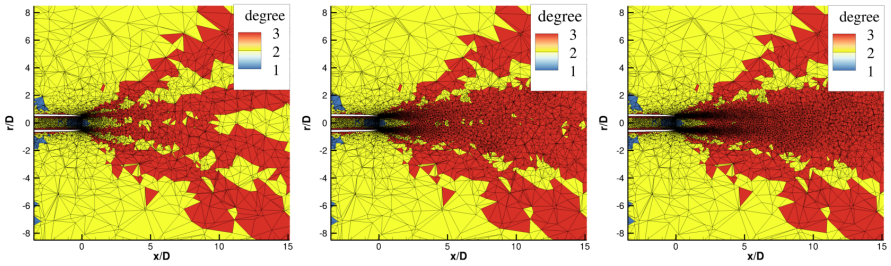

Fig. 3: hpDG/ZDES simulations of the PPRIME nozzle. Zoom on the nozzle exit region and early jet plume for the three *hp*-adapted meshes, *hp*G1 at the left, *hp*G2 in the middle, *hp*G3 at the right.

The mesh *hp*G1 mostly displays $p = 2$ and $p = 3$ elements in the jet plume, except for the exit of the nozzle, which is discretized with $p = 1$ elements. The external part of the shear layers present $p = 2$ elements since the smoothness estimator in previous RANS simulations had detected non-smooth features in this region, and had prevented the algorithm from increasing the polynomial degree in this zone.

A concentration of the h-refinement can be observed around the potential core. The zone relevant for unsteady ZDES simulations is the mixing layer zone where the vortices develop from the lip of the nozzle. In this region the maximum polynomial degree $p = 3$ is selected by the algorithm. As seen from TGV tests in [82], this property is desirable because high-order DG discretizations describe the turbulence more accurately than low order discretizations with an equivalent number of degrees of freedom.

The hp-adapted meshes hpG2 and hpG3 increase the degree of $p = 2$ elements located in the jet plume to the maximum $p = 3$, especially on the axis of the jet. Globally, the polynomial degree distribution remains the same for the three meshes hpG1, hpG2 and hpG3, since the RANS adaptation had already broadly identified the flow regions of interest and provided a reasonable initial discretization.

The most important difference between the three hp-meshes resides in the size of the elements in the jet plume. The mixing layer, presenting strong vortical structures needing very fine resolutions to be adequately captured, is progressively h-refined, since the maximum polynomial degree has already been reached. As the new meshes are properly partitioned, the simulations are balanced with respect to the number of mesh elements. However, higher degree computations would need *ad-hoc* p load balancing techniques, which are not the subject of the present paper, but will be addressed in future work. We also note that very high-order unstructured DG discretizations can present robustness or efficiency issues, which might not be compatible with applications in a challenging industrial context.

In figure 4 we display the distribution of the error estimator for the hpG1 and hpG2 discretizations, which drives the refinement for the discretizations hpG2 and hpG3, respectively.

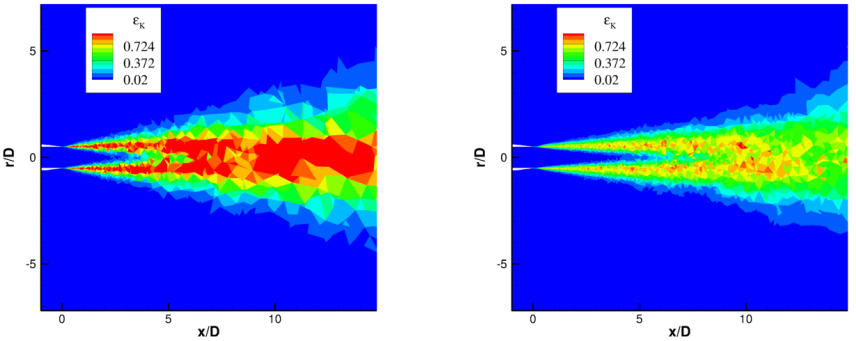

Fig. 4: hpDG/ZDES simulations of the PPRIME nozzle. Close-up view of the error estimator distribution in the nozzle exit region and early jet plume for the hp-adapted meshes, hpG1 on the left and hpG2 on the right.

The error estimator is found to correctly identify the most unresolved zones of the flow and detects the turbulent shear layers of the jet. In particular we notice a growing intensity of the error estimator in zones corresponding to high rms values of the velocity, whose profiles will be presented in the following sections, in figures 10 and 12. These regions are mainly the lipline and the centerline at the end of the potential core. This behavior is reflected by the distribution of the degrees of freedom in figure 3, where the elements in the lipline are h-adapted in both the adaptive steps (as they already reached the maximum polynomial degree $p = 3$), and the elements in the centerline are first mainly p-adapted (hpG2) and then h-adapted (hpG3). A difference with respect to the steady RANS adaptations performed in previous work [38] on the same configuration lies in the concentration of the dofs obtained by the adaptation. Indeed the most refined region for scale-resolving simulations is mainly located in the turbulent shear layers, while for RANS equations it is mainly identified in the high mean velocity gradient zone of the potential core.

4.2.2 Qualitative instantaneous field analysis

A first qualitative assessment of the results is conducted by the means of the visualizations of the instantaneous flow field for the three hp-meshes hpG1, hpG2, hpG3, which are presented in figure 5 and 6 and compared.

Figure 5 describes the instantaneous fields of temperature (colour) and pressure fluctuations (grey scale), for the meshes hpG1 with 11.6 millions dofs (top), hpG2 with 18.9 millions dofs (middle) and hpG3 with 31.7 millions dofs (bottom). These pictures show how the most resolved computation captures smaller turbulent structures compared to the two coarser simulations, thanks to the hp-adaptation in the zones of interest of the jet. Moreover we notice how the use of a finer grid resolution in the jet flow leads to a slower jet development (and a longer potential core). This trend will be further discussed in the next section.

In figure 6, vorticity snapshots are shown for three different sections $x/D = 1, 2, 3$ downstream the nozzle (plots from the left to the right), for hpG1, hpG2, hpG3 computations (top, middle, bottom rows). hpG1 displays larger structures than hpG2 and hpG3 resolutions for $x/D = 1$, while solutions in between hpG2 and hpG3 are almost indistinguishable. More consistent differences can be found for locations further downstream the exit nozzle. While for hpG1 the turbulent structures are barely captured at $x/D = 2, 3$, hpG2 displays a sharp representation of small structures, even more so for hpG3.

In figure 7 instantaneous snapshots of the turbulent viscosity near the nozzle lip for the three discretizations hpG1, hpG2 and hpG3 are studied. We observe a spot of high turbulent viscosity values immediately at the exit of the nozzle, up to a distance of $x/D \sim 0.1$, that corresponds to the turbulent viscosity which is transported downstream from the RANS nozzle boundary layer. However, the turbulent viscosity returns to low values quickly. Further downstream, for $x/D > 0.1$, relatively low values of the DES turbulent viscosity are observed, followed by a rapid increase in the shear layer region corresponding

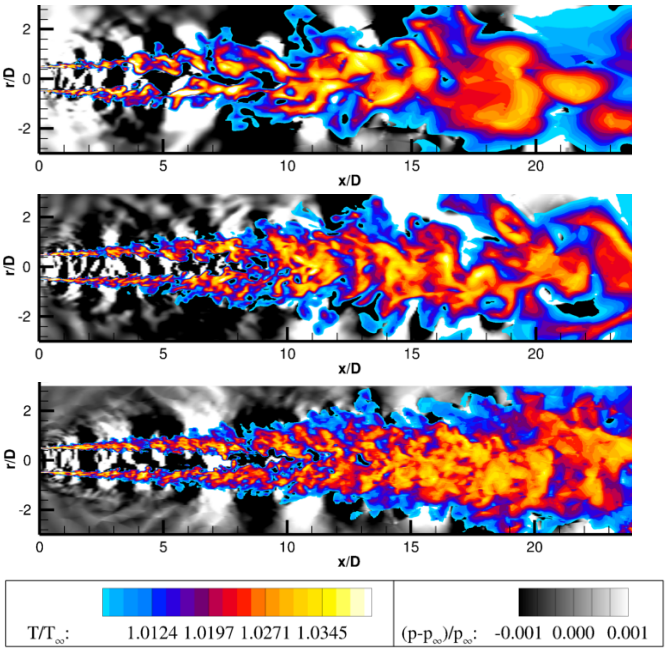

Fig. 5: hpDG/ZDES simulations of the PPRIME nozzle. Iso-contours of temperature T/T_∞ in colored-scale and $(p - p_\infty)/p_\infty$ in greyscale. Zoom of the *hp*G1 mesh (top), the *hp*G2 mesh (center) and the *hp*G3 mesh (bottom).

to the development of the three-dimensional turbulent structures. Comparing the three panels in figure 7, we observe that the turbulent viscosity values progressively decrease with the increase of the spatial resolution introduced by the adaptive approach, as the adaptation process leads to an improved representation of the finer turbulent scales and lower levels of modeled viscosity. This behavior is expected, as the turbulent viscosity provided by the model in the DES regions scales with the square of the characteristic mesh element size. We also remark that the *hp*G1 simulation and, to a lesser extent, the *hp*G2 simulation present an early transition which might be forced by the coarse resolution in this area.

4.2.3 Quantitative data analysis

In this part, the simulation results are analyzed in terms of mean and fluctuating velocity profiles in the various regions of interest of the jet flow. First we study the quality of the solution at the exit of the nozzle, and the boundary layer velocity profile is extracted in figure 8 at $x/D = 0.04$.

For the three simulations, the velocity profiles for *hp*G1, *hp*G2, *hp*G3, respectively in blue, red, black straight lines, are found to match experimental data in squared symbols and the RANS simulation on *hp*G1 in dotted lines. Note that in the proximity of the nozzle exit, no substantial differences can

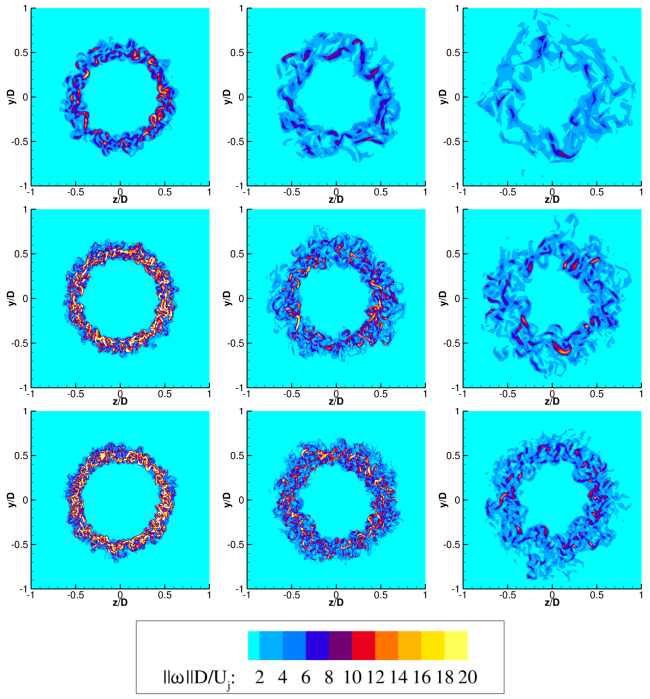

Fig. 6: hpDG/ZDES simulations of the PPRIME nozzle. Iso-contours of vorticity at $x/D = 1, 2, 3$ (from left to right) for *hp*G1 (top), *hp*G2 (middle), *hp*G3 (bottom).

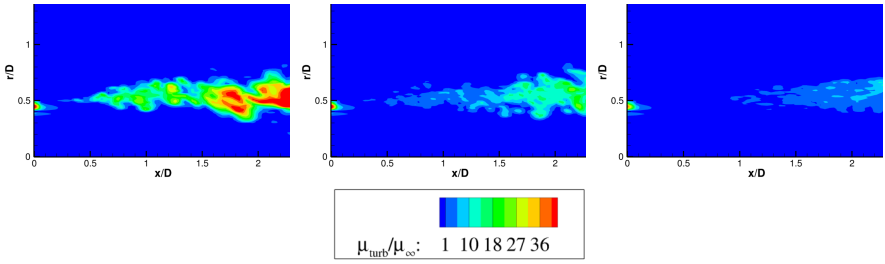

Fig. 7: hpDG/ZDES simulations of the PPRIME nozzle. Close-up view of the turbulent viscosity contours in the nozzle exit region for the three *hp*-adapted meshes, *hp*G1 (left), *hp*G2 (middle), *hp*G3 (right).

be found between *hp*G1, *hp*G2, *hp*G3 hybrid RANS/LES results, because the flow features here mainly depend on zones solved with RANS equations, which are similarly resolved for the three discretizations.

We note that a turbulent velocity profile is obtained at the nozzle exit due to the RANS modeling inside the nozzle, but turbulent injection were not considered in this work, thus some discrepancies between the present results

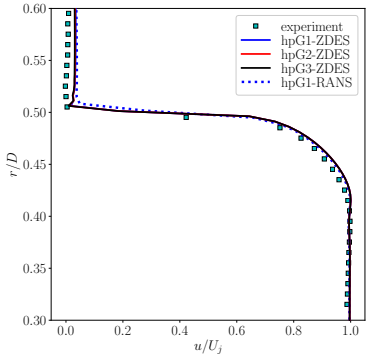

Fig. 8: hpDG/ZDES simulations of the PPRIME nozzle. Boundary layer velocity profile at $x/D = 0.04$. Comparison between *hp*-adaptive and reference results.

and experimental results or computational results with turbulence tripping inside the nozzle are expected.

	#dofs (M)	spatial discr.	turbulence modeling	turbulent injection	simulated duration (D/U_j)	mesh type
Brès et al. G1 [79]	16	FV-2o	LES-Vreman	yes	2000	unstruct hexa
Brès et al. G2 [79]	69	FV-2o	LES-Vreman	yes	1150	unstruct hexa
Gand & Huet G1 [80]	48	FV-2o	ZDES mode 2	no	300	struct hexa
Gand & Huet G2 [80]	154	FV-2o	ZDES mode 2	no	300	struct hexa
Shur et al. G1 [83]	8.4	FV-ho	RANS profile+ILES	no	250	struct hexa
Shur et al. G2 [83]	23	FV-ho	RANS profile+ILES	no	250	struct hexa
Lorteau et al. G1 [46]	78	DG-4o	LES-Smagorinsky	no	180	unstruct tetra
Lorteau et al. G2 [46]	165	FV-2o	LES-Smagorinsky	no	250	unstruct tetra
*hp*G1 [present]	11.6	*hp*-DG	ZDES mode 0+1	no	150	unstruct tetra+prism
*hp*G2 [present]	18.9	*hp*-DG	ZDES mode 0+1	no	150	unstruct tetra+prism
*hp*G3 [present]	31.7	*hp*-DG	ZDES mode 0+1	no	150	unstruct tetra+prism

Table 1: hpDG/ZDES simulations of the PPRIME nozzle. Comparison between parameters in simulations in the literature and present *hp*-adapted simulations.

The mean streamwise velocity profiles on the jet axis $r/D = 0$ and on the lipline $r/D = 0.5$, are compared in figures 9 and 10 to experimental and numerical results obtained by Brès et al. [79] in green lines, Gand & Huet [80] in magenta lines, Shur et al. [83] in orange lines, and Lorteau et al. [46] in cyan lines, whose parameters and numerical set-up are described in table 1. Dotted lines represent coarse grids for each reference, while dashed lines represent fine grids. Shur et al. and Lorteau et al. show the mean velocity profile along the streamwise direction at the radial position corresponding to the peak of rms velocity instead of the lipline velocity. However the peak of the rms velocity is found very close to $r/D = 0.5$, and the two quantities can be directly compared.

Before further analyzing the results, the reference data and related numerical techniques and modeling approaches are briefly reviewed. Brès et al. used a second order Finite Volume approach on unstructured hexahedral-dominant grids, obtained with an *a priori* isotropic mesh adaptation procedure, where it is not an error estimator that guides the process, but an *a priori* knowledge of the physical phenomenon. Starting from a structured mesh with a low number of elements, several embedded zones of refinement with specific target length scale are defined by the user and enforced iteratively by the adaptation tool. Moreover further mesh refinement is added inside the nozzle in the near-wall zone. Regarding their LES strategy, the Vreman subgrid model is used, coupled with an equilibrium wall model inside the nozzle, which allows for selecting element sizes significantly larger than $y^+ = 1$ at the wall. They also used synthetic-turbulence boundary conditions to model the boundary-layer trip present in the experiment on the internal nozzle surface.

Gand & Huet adopted hexahedral structured meshes with a second-order FV scheme, modeling the turbulence with ZDES mode 2 and ZDES mode 3 approaches. Here we consider only their ZDES mode 2 results, since both ZDES mode 0+1 employed in this work and ZDES mode 2 aim at modeling the boundary layers inside the nozzle with a RANS approach without a tripping of turbulent structures and thus account for a similar modeling approach.

Shur et al. employed high-order FV schemes on structured meshes. They used a two-stage simulation procedure in which the inflow velocity profile was imposed from a RANS solution previously obtained on a coupled nozzle/jet plume RANS simulation, excluding the geometry from the ILES computation. This allowed them to reproduce the effect of the boundary layer considerably reducing the high cost of a coupled nozzle/jet plume LES. Because of this, a direct comparison between the number of dofs employed in their simulations and in our adaptive DG *hp*-meshes cannot be done in a straightforward manner. However it is still interesting to compare our results with those obtained by Shur et al. as in both cases the nozzle exit profile is obtained from RANS modeling approaches.

Lorteau et al. adopted a fourth-order DG approach on fully tetrahedral meshes. No tripping procedure was employed, and the Smagorinsky subgrid model was used for LES. Their only DG simulation results (G1) are shown

in dotted lines. The shear layer is here laminar close to the nozzle exit, as no turbulent injection technique has been considered to trigger the transition to turbulence within the nozzle.

For each of the four numerical references, results obtained on two grid resolutions (except for Lorteau for which we have only one DG resolution) are extracted and compared to the present *hp*-adaptive results.

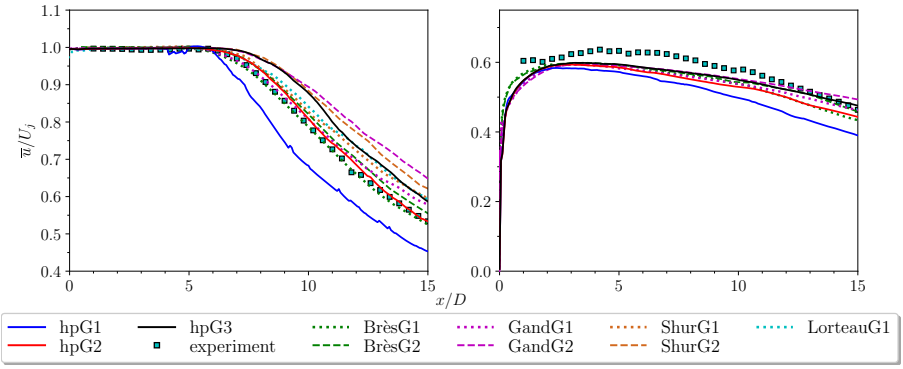

Fig. 9: hpDG/ZDES simulations of the PPRIME nozzle. Mean streamwise velocity profiles on the jet axis $r/D = 0$ (left) and on the lipline $r/D = 0.5$ (right). Comparison between *hp*-adaptive and reference results.

The first observation that can be made is that refining (in h and p) the jet plume, the velocity decay on the jet axis becomes slower, leading to longer potential cores (as already observed in figure 5). Surprisingly, we can observe how the adaptive simulation *hp*G2 seems to provide closer results to the experiment, while the more refined *hp*G3 mesh overestimates the length of the potential core. Even though this results could seem unexpected, this behavior has been already pointed out by Shur et al. in [83] (in orange lines), and can be found in results from Gand & Huet [80] (in magenta lines) as well. The *hp*G3 fine mesh provides an axial mean velocity profile in very close accordance with their most refined simulations. It should be reminded that these two modeling approaches are very similar to that employed in this work. However, a similar overestimation of the length of the potential core is also observed in pure LES simulations by Brès et al. [79] (in green lines) in a less marked manner, and by Lorteau (in cyan lines). The reasons for this overestimation of the jet potential core length are still not clear. Shur et al. hypothesized two reasons for this behavior: one is that it might be caused by the use of ILES, while the other is that it might be caused by the feedback loop between jet turbulence and nozzle not accurately reproduced by the system of boundary conditions. The second observation would be valid also for our ZDES mode 0+1 model, because the small-scale variations of the turbulent flow cannot go back upstream and interact with the interior of the nozzle, which is modeled in RANS. Lorteau et al. attributed this overestimation to the lack of an appropriate turbulent

injection technique to trigger the transition to turbulence within the nozzle, as it happens in the experiment.

Even though a formal answer has not been found, we think that a combination of several effects could be the cause of this behavior. In particular the lack of turbulent injection: the turbulent transition and formation of jet coherent structures here occurs in the shear layer, outside the nozzle. This consists in the processes of vortex rolling-up and pairing, after which three-dimensional turbulence appears. This may affect both the flow and the acoustic solution in different ways [46, 79, 84]. We remind here that the experiment presents a fully turbulent boundary layer, after triggering the turbulence inside the nozzle with a strip. In this case, the boundary layer turbulent structures formed inside the nozzle are likely to influence the dynamics of shear-layer structures formed in the vicinity of the nozzle exit. A similar tripping technique could be considered as future work in our simulations in order to elucidate its effect on the jet plume flow dynamics and check if the simulations converge towards the experimental results when the mesh is refined or adapted. It is also possible that the resolution is still insufficient. In this case, a fourth more refined simulation (not performed because of limited computational resources) should be performed in order to assess the flow properties in terms of mean and fluctuating profiles and verify the trends observed in the previous three *hp*-simulations.

Compared to reference simulations, the axial mean velocity is in very close accordance with the most refined simulations by Gand & Huet and Shur et al., while for $x/D > 10$ the decay of the velocity is faster for *hp*G3. This is due to the a lower resolution in this zone with respect to the two authors, suggesting that a further adaptation step providing additional refinement for $x/D > 10$ would eventually slow the decay of the centerline velocity. Moreover, we remark that, in accordance with the observations by Gand & Huet [80], the relatively short simulation time might also introduce some uncertainties in the results corresponding to this region, which is characterized by low frequency phenomena.

An observation of the mean velocity profile on the lipline in the right panel of figure 9, reveals the impact that grid refinement has in the development of the shear layer, especially for $x/D > 2$. Here grid refinement yields an increased velocity along the lipline, which tends towards the experimental profile.

In figure 10 we show rms streamwise velocity profiles in the centerline (left) and in the lipline (right). Looking at the centerline velocity profiles, we notice that the profile is not smooth, but presents spurious peaks. These peaks are pronounced for the coarse simulation *hp*G1, while they tend to decrease in intensity thanks to the adaptive grid refinement. This aspect can originate from the DG scheme, where the solution is discontinuous across elements and the polynomial approximating the solution can have very sharp shapes near the interfaces of very coarse elements. Similar numerical oscillations have been already observed in the DG literature [74, 85–87] when using coarse discretizations. Usually these oscillations disappear when increasing the resolution. Numerical discontinuities at the interface of coarse elements for LES-DG

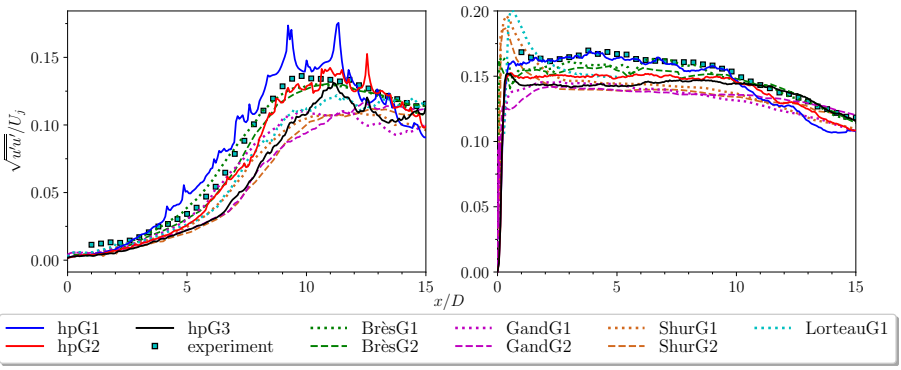

Fig. 10: hpDG/ZDES simulations of the PPRIME nozzle. Root-mean square of the streamwise velocity fluctuation profiles on the jet axis $r/D = 0$ (left) and on the lipline $r/D = 0.5$ (right). Comparison between *hp*-adaptive and reference results.

computations have been observed as well in *a priori* studies by Beck et al. [88], where a DNS solution of a decaying homogeneous isotropic turbulence was projected on a DG/LES grid, which is representative of the "exact" LES solution for DG. This projected solution presented discontinuous features in the flow field at the interface of the LES grid elements, which indicates that the discontinuities or peaks are a natural part of DG/LES discretizations, when no explicit filtering procedure is considered.

It is also likely that the numerical peaks in the left panel of figure 10 partly originate from the statistical sampling which is low at the centerline due to the inability of performing a spatial azimuthal averaging at this location.

This behavior is improved thanks to mesh adaptation, and peaks in the solution gradually disappear for *hp*G2 and *hp*G3. These numerical artefacts in the solution are not apparent for lipline plots in the right panels of figures 9 and 10, as well as velocity profiles in figures 11 and 12, probably due to the better sampling of the solution which is averaged in the azimuthal direction and/or a better resolution in the lipline area.

The small peak seen in the lipline velocity rms profile around $x/D = 0.5$ is very similar for *hp*G1 and *hp*G2, meaning that in the zone close to the nozzle exit the two meshes display the same flow features probably due to the similar size of the elements in this region. A lack of resolution just downstream of the jet exit seems to accelerate the mixing-layer transition, resulting in higher axial (in the centerline) and peak values (in the lipline) of turbulence intensities for the *hp*G1 simulation compared to the more refined simulations *hp*G2 and *hp*G3, as can be seen both in the right and the left panel of figure 10 for $x/D > 0.5$. For the finer simulations we observe an underestimation of the turbulence intensities with respect to experiments in the early phases of the jet development for $x/D < 10$. This behavior is observed as well for reference

simulations. Dotted curves, representing coarser meshes, show lower rms levels than dashed curves, representing the finest mesh for each reference. This is particularly evident for simulations by Shur et al. and Gand & Huet. The decrease in axial/peak rms velocities for $x/D < 10$ can be directly associated with the longer potential core length for fine simulations [89]. However, over the two adaptation steps, the rms levels move progressively closer to the reference experimental data for $x/D > 10$, in the region downstream of the potential core. This has been observed as well in the other numerical reference simulations, and is consistent with the fact that a lower resolution also leads to lower rms axial/peak velocities downstream of $x/D = 10$.

The irregular axial rms profiles for $x/D > 10$ suggest that statistics could be collected for a longer sampling period to provide smoother plots. In fact, from $x/D > 10$ the flow has a longer eddy turnover time than the zone close to the exit nozzle. Moreover rms quantities need more time to converge compared to average quantities, and axial quantities cannot be azimuthally averaged.

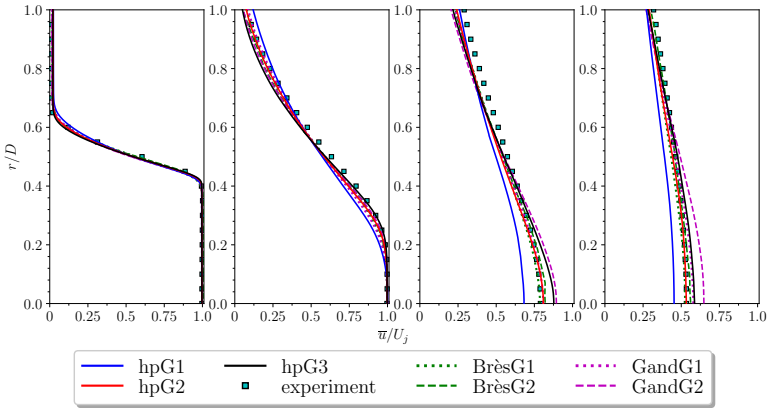

Fig. 11: hpDG/ZDES simulations of the PPRIME nozzle. Mean streamwise velocity profiles on different locations in the jet plume $x/D = 1, 5, 10, 15$ (from left to right). Comparison between *hp*-adaptive and experimental results.

Figures 11 and 12 show the mean and rms streamwise velocity radial profiles at different axial locations downstream the nozzle exit. For the locations $x/D = 1, 5$ closer to the nozzle exit, we see an improvement in the prediction of the mean velocity profile during the mesh adaptation process, and a lower shear layer thickness of the jet is observed for *hp*G2 and *hp*G3 simulations. At locations $x/D = 10, 15$, similar observations to those made for the centerline profile in figure 9 can be made. *hp*G1 clearly underestimates the mean velocity level close to the centerline. *hp*G2 seems to provide results in close agreement with experimental results, while *hp*G3 simulation overestimates the velocity for $r/D < 0.5$ in both the locations, especially at $x/D = 15$.

However, *hp*G3 profiles at $x/D = 10$ closely matches to the fine simulation by Gand & Huet, and displays an intermediate value between the coarse and the fine simulations by Gand & Huet for $x/D = 15$. This confirms once again the trend of overestimation of the axial velocity when refining the mesh, already observed by other authors who performed numerical simulations on two different grid resolutions.

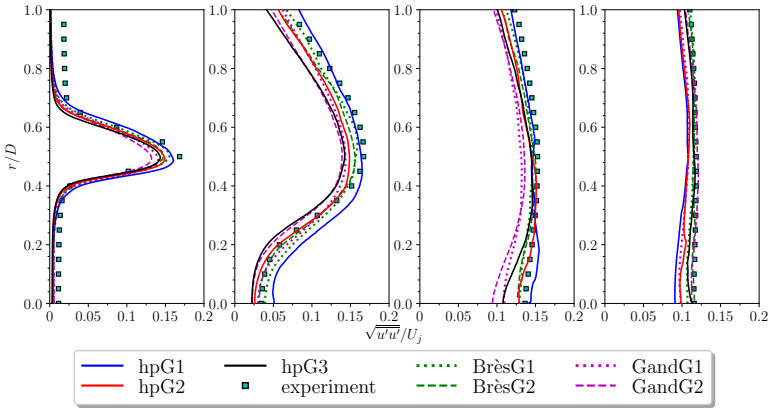

Fig. 12: hpDG/ZDES simulations of the PPRIME nozzle. Root-mean square of the streamwise velocity fluctuation profiles on different locations in the jet plume $x/D = 1, 5, 10, 15$ (from left to right).

From the profiles of rms velocity fluctuations, we see that *hp*G2 and *hp*G3 provide lower levels of turbulent intensities with respect to *hp*G1 results, for $x = 1, 5, 10$. Since the simulation does not present explicit turbulent structures at the nozzle exit, lower levels of rms velocity are expected in the vicinity of the nozzle. The higher levels of the *hp*G1 simulation, apparently closer to the experimental results than *hp*G2 and *hp*G3, are attributed to a lack of resolution, which fictitiously provides a better solution (as observed in the right panel of figure 10). The same behavior is observed for $x/D = 5$ and $x/D = 10$, yet the *hp*G1 simulation shows a substantial overestimation of the rms levels when getting closer to the axis. This is related to the coarse grid-induced rapid growth of the shear layer due to the RANS-to-LES transition. This produces larger vortices, providing a higher kinetic energy.

All these observations agree with the results by Brès et al. and Gand & Huet, respectively displayed with green and magenta lines, comparing the coarse (dotted lines) and the fine (dashed lines) simulations. The rms velocity profile at $x/D = 15$ matches more closely the experiment as the mesh is refined, as can be observed also for simulations by Brès et al. and Gand & Huet. This emphasizes the ability of the *hp*-adaptation strategy to detect and refine the turbulent structures in the far wake and improve in turn the estimation of the turbulent fluctuations.

Overall good results, in line with numerical references, have been obtained with the present unstructured *hp*-adaptive strategy with a reasonable amount of degrees of freedom. The most refined *hp*-adapted mesh employed here counts a lower number of dofs than both the unstructured DG-$p3$ simulations by Lorteau [46] and the structured FV simulations by Gand & Huet, while achieving very close results.

Observations and comparisons with Brès et al. and Shur et al. in terms of number of dofs employed and achieved accuracy should be analyzed with caution. This is because the former employed turbulent injection which gives explicit turbulent structures inside the nozzle, as well as a wall model for LES which allows for defining a coarser mesh inside the nozzle compared to our approach. The latter did not mesh the interior of the nozzle, yielding an overall reduction of dofs compared to approaches with an explicit meshing of the nozzle interior.

4.3 Far-field acoustics computational set-up

For the three *hp*-meshes, we performed computations of the far-field noise on two arrays of microphones: a cylindrical array located at 14.3D from the jet axis and a polar array located at 50D from the nozzle exit. Each angle of observation counts 36 azimuthal microphones.

The Ffowcs Williams-Hawkings (FW-H) surface integral method is used to estimate the far-field noise implemented in the KIM software developed at ONERA.

The high-order solution is interpolated onto a cylindrical-conical-cylindrical surface enclosing the nozzle geometry and the noise surfaces, as shown in figure 13, and stored every $\Delta t_{\text{FW-H}} = 0.033 t_c$, which means every five flow statistics collections ($\Delta t_{\text{sampl}} = 0.0067 t_c$). This surface is closed at the downstream extremity, and the additional flux terms proposed by Rahier et al. [56] are used in the FW-H formulation, in order to improve the stability of the noise computed from the different surfaces, especially in the low frequency part of the spectra.

The instantaneous flow field is interpolated on four different surfaces (S1, S2, S3, S4) of revolution in figure 13, which differ by their radial extent, in order to assess the effects of the position of the surfaces on the acoustic results. The radii of the upstream cylinder-shaped control surfaces S1, S2, S3, S4 are $r/D = 0.68, 1, 1.35, 1.7$. Truncated cones with spreading rate $\alpha = 0.15$ (final radii $r/D = 3.68, 4, 4.35, 4.72$ respectively for S1, S2, S3, S4) connect the upstream cylinders with downstream cylinders. The closing surfaces D1, D2, D3 are located at $x/D = 20, 25, 30$.

Once assessed a global independence of acoustic results from choice of the surface employed to perform the integration, only the results obtained by signals extrapolated from the surface S1-D3 are presented in this section.

The total sampling time for the pressure on the FW-H surfaces is the same as accumulated statistics $T_{\text{stats}} = 150 t_c$. However, due to geometrical transients at the beginning and end of the acoustic extrapolation, the exploitable

interval reduces to around $130t_c$. Although aware of the relatively short time of collection of the pressure signals, the overall behavior of the *hp*-adaptation on acoustic results is still representative. Some examples of relevant simulations performed over similar amounts of non-dimensional units can be found in [89] for the finer grids and in [46] for similar nozzle configurations.

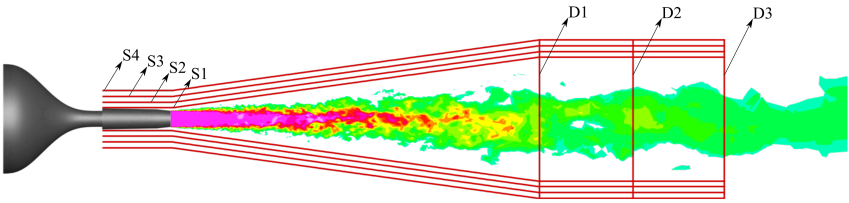

Fig. 13: hpDG/ZDES simulations of the PPRIME nozzle. Schematics of the acoustical set-up. Location of the FW-H surfaces.

4.4 Far-field acoustic results

The Power Spectral Density (PSD) is computed on the microphones at different angles of observation, from $\theta = 20°$ to $\theta = 90°$, and is azimuthally averaged on the 36 azimuthal microphones for each angle of observation to compensate for the shorter time signal in the simulations with respect to experiments and reference LES results. The Welch method is used to estimate the PSD [90]. A Hann window is applied to each block composed of 1000 sampled data and an overlap of 75 % is imposed.

The PSD is reported in [dB/St], as a function of frequency expressed in Strouhal $St = fD/U_j$, following the same non-dimensionalization used in the experiment and the LES reference results by Brès et al. The resulting spectra obtained on the three *hp*-adapted meshes at $\theta = 90°, 60°, 20°$ are showed in figure 14, *hp*G1 in blue, *hp*G2 in red, *hp*G3 in black, and compared with experimental results in squared symbols and the LES reference results by Brès et al. in dotted green lines.

In the first place we observe that the noise level is overestimated for the coarse *hp*G1 and the medium mesh *hp*G2 for all the observation angles. The use of more refined meshes globally leads to lower levels of the PSD, especially in the low frequency range. This behavior is in accordance with the lower turbulence intensities pointed out in figure 10 when increasing the resolution. This results in a good prediction of the far-field noise levels by the finer *hp*G3 mesh in the medium frequency range, and a slight underestimation in the low-frequency range of the spectra for low angles of observations. This behavior is expected, as the turbulent intensities predicted by the *hp*G3 mesh in the axis just downstream the potential core, which are correlated to the strong low frequency noise emitted at low angles, are slightly underestimated as compared to experimental measurements.

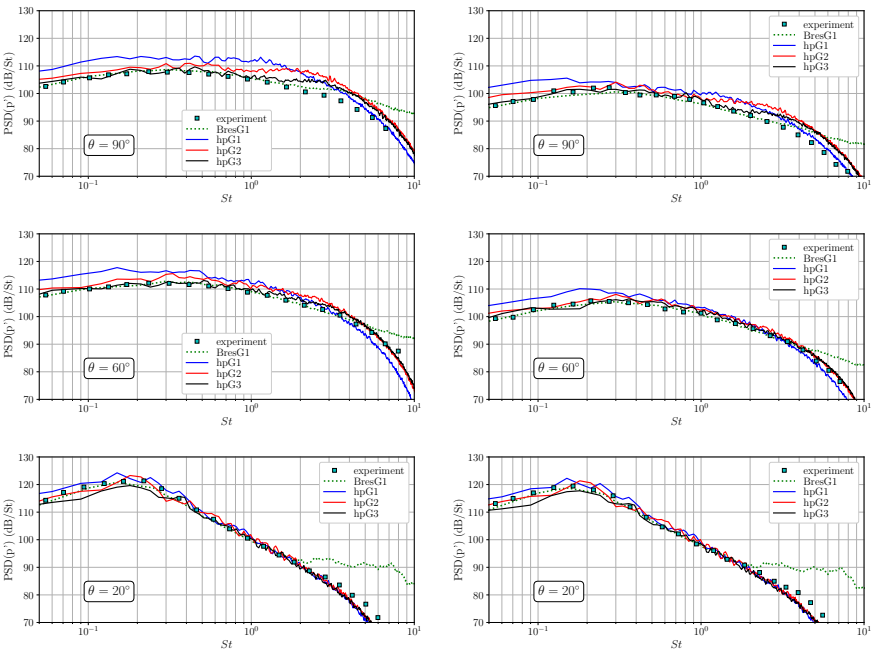

Fig. 14: hpDG/ZDES simulations of the PPRIME nozzle. PSD of the pressure on the cylindrical microphone array of radius r = 14.3D (left) and on the polar microphone array at 50D from the nozzle exit (right) for different angles of observation.

Moreover, for high angles of observation, the PSD is overestimated in the medium frequency range for all the three resolutions. This is due to the vortex rolling and pairing which in our simulations, performed without turbulent injection or tripping techniques in the nozzle, occurs outside the nozzle and causes increased noise levels with respect to the experiment. However, we can observe that globally *hp*-adaptation leads to spectra which are in closer agreement with the experiment, and a less pronounced bump in the medium/high frequency range.

Finally, the Overall Sound Pressure Level (OASPL) in [dB] is computed in the frequency bandwidth $0.05 < St < 3$, for both the cylindrical and the polar array (figure 15). Very similar observations to those made for the spectra can be made for the OASPL levels. Globally, the OASPL is overestimated for both the coarse and the medium meshes, especially for high angles. While still slightly overestimating the noise levels by about 1 dB in the polar array and 2 dB in the cylindrical array for high angles of observation, due to the vortex pairing phenomenon, the fine *hp*G3 mesh provides global results in good agreement with the experiment. For low angles of observation $\theta < 40°$, the noise levels are underestimated by 1-2 dB, due to the underestimation of the low frequencies in the PSD spectrum.

Overall, the adaptation process has significantly improved the estimation of the far-field noise. These results are providing a reliable prediction of the trend that the acoustic levels follow when increasing the resolution. However, as observed by Gand & Huet [80] for the fluid flow results, longer simulation times ($T_{\text{stats}} > 300D/U_j$) should be considered in order to decrease the uncertainties, especially due to the low frequency phenomena characterizing the jet evolution.

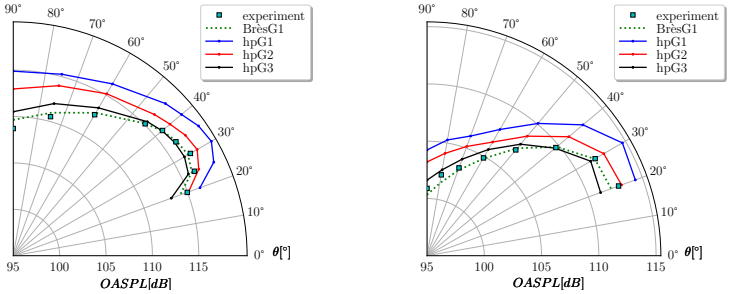

Fig. 15: hpDG/ZDES simulations of the PPRIME nozzle. OASPL on the cylindrical microphone array of radius r = 14.3D (left) and on the polar microphone array at 50D from the nozzle exit (right) for different angles of observation.

5 Conclusions

In the present paper, an *hp*-adaptation strategy suitable to discontinuous Galerkin methods on hybrid prismatic/tetrahedral meshes has been proposed for scale-resolving simulations of turbulent fluid flow problems based on a hybrid RANS/LES approach relying on a combination of ZDES mode 0 and 1. The error estimator based on both the measure of the energy contained in the highest order polynomial modes and the jumps of the solution at the element interfaces, used in combination with a smoothness estimator, has been found to correctly identify the flow regions of interest in a hybrid RANS/LES context, that are then marked for *hp*-adaptation. *hp*-adapted DG computations of the PPRIME nozzle at $Re_D = 10^6$ have been carried out for a ZDES configuration, and the impact of increased resolution has been analyzed for three adapted meshes *hp*G1, *hp*G2, *hp*G3 presenting respectively 11.6, 18.9, 31.7 million dofs. Quantitative results compared fairly well to numerical references, obtaining overall close results to classical FV schemes on structured meshes and non-adaptive DG methods, with a reduced number of degrees of freedom. The acoustic analysis of the far-field propagated jet noise has been as well performed on the *hp*-adapted meshes using a FW-H method, showing a fair agreement for the adapted simulations compared to reference acoustic spectra and OASPL in the far-field, within an uncertainty range due to the short performed simulation time.

However, some discrepancies can be found in the flow field obtained on the finest adapted meshes, with respect to the results obtained by the experimental measurements. In particular, longer potential cores, associated with lower turbulence intensities, are found when increasing the resolution. This appears to be a recurrent issue in the literature, especially when dealing with simulations in which the turbulence is not explicitly triggered inside the nozzle.

In future work, turbulent injection/tripping techniques will be considered, in order to assess the impact of the nozzle interior boundary layer turbulent structures on flow field and far-field acoustic results in the context of *hp*-adaptive DG methods. The development of anisotropic features in the *h*-adaptive procedure is also planned in order to automatically adapt the mesh in the boundary and shear layers and further improve the adaptation procedure for highly turbulent flows, applied both to RANS and scale-resolving simulations.

Acknowledgments. The authors gratefully acknowledge the support provided by Dr Gilles Rahier for the aeroacoustic analysis. The authors would like to thank as well Dr Fabien Gand, Dr Maxime Huet and Dr Mathieu Lorteau from ONERA for providing access to numerical data and fruitful discussions on jet simulations, and Dr Fabio Naddei from ONERA for his valuable help in DG-adaptive strategies.

Declarations.

- **Funding**: This work has been performed using HPC resources from GENCI-CINES (Grant 2021-A0102A11470) and internal ONERA and Airbus HPC resources.
- **Conflict of Interest**: The authors declare that they have no confict of interest.
- **Ethical approval**: Not applicable.
- **Informed consent**: Not applicable.

References

[1] Chaouat, B.: The state of the art of hybrid RANS/LES modeling for the simulation of turbulent flows. Flow, Turbulence and Combustion **99**(2), 279–327 (2017)

[2] Sagaut, P., Deck, S., Terracol, M.: Multiscale & multiresolution approaches in turbulence. 2006 London. UK: Imperial College Press (2006)

[3] Spalart, P.R.: Comments on the feasibility of LES for wings, and on a hybrid RANS/LES approach. In: Proceedings of First AFOSR International Conference on DNS/LES (1997). Greyden Press

[4] Spalart, P.R., Deck, S., Shur, M.L., Squires, K.D., Strelets, M.K., Travin, A.: A New Version of Detached-Eddy Simulation, Resistant to Ambiguous

Grid Densities. Theoretical and Computational Fluid Dynamics **20**(3), 181–195 (2006)

[5] Deck, S.: Recent improvements in the Zonal Detached Eddy Simulation (ZDES) formulation. Theoretical and Computational Fluid Dynamics **26**(6), 523–550 (2012)

[6] Karniadakis, G., Sherwin, S.: Spectral/hp Element Methods for Computational Fluid Dynamics. Oxford University Press, ??? (2013)

[7] Dolejší, V., Feistauer, M.: Discontinuous Galerkin method. Analysis and Applications to Compressible Flow. Springer Series in Computational Mathematics **48** (2015)

[8] Mavriplis, C.: A posteriori error estimators for adaptive spectral element techniques. In: Proceedings of the Eighth GAMM-Conference on Numerical Methods in Fluid Mechanics, pp. 333–342 (1990). Springer

[9] Persson, P., Peraire, J.: Sub-cell shock capturing for discontinuous Galerkin methods. In: 44th AIAA Aerospace Sciences Meeting and Exhibit, p. 112 (2006)

[10] Gassner, G., Altmann, C., Hindenlang, F., Staudenmeier, M., Munz, C.: Explicit Discontinuous Galerkin Schemes with Adaptation in Space and Time. 36th CFD/ADIGMA course on hp-adaptive and hp-multigrid methods, VKI LS (2009)

[11] Remacle, J.-F., Flaherty, J.E., Shephard, M.S.: An adaptive discontinuous Galerkin technique with an orthogonal basis applied to compressible flow problems. SIAM review **45**(1), 53–72 (2003)

[12] Dolejší, V.: hp-DGFEM for nonlinear convection-diffusion problems. Mathematics and Computers in Simulation **87**, 87–118 (2013)

[13] Leicht, T., Hartmann, R.: Error estimation and hp-adaptive mesh refinement for discontinuous Galerkin methods. In: Adaptive High-order Methods in Computational Fluid Dynamics, pp. 67–94. World Scientific, ??? (2011)

[14] Wang, L., Mavriplis, D.: Adjoint-based h–p adaptive discontinuous Galerkin methods for the 2D compressible Euler equations. Journal of Computational Physics **228**(20), 7643–7661 (2009)

[15] Burgess, N., Mavriplis, D.: An hp-adaptive discontinuous Galerkin solver for aerodynamic flows on mixed-element meshes. In: 49th AIAA Aerospace Sciences Meeting Including the New Horizons Forum and Aerospace Exposition, p. 490 (2011)

[16] Chalmers, N., Agbaglah, G., Chrust, M., Mavriplis, C.: A parallel hp-adaptive high order discontinuous Galerkin method for the incompressible Navier-Stokes equations. Journal of Computational Physics: X **2**, 100023 (2019)

[17] Deck, S.: Zonal-Detached-Eddy Simulation of the Flow Around a High-Lift Configuration. AIAA Journal **43**(11), 2372–2384 (2005)

[18] Brunet, V., Deck, S.: Zonal-detached eddy simulation of transonic buffet on a civil aircraft type configuration. In: Advances in Hybrid RANS-LES Modelling, pp. 182–191. Springer, Corfu, Greece (2008)

[19] Brunet, V., Deck, S.: Zonal-detached eddy simulation of a civil aircraft engine jet configuration. In: Progress in Hybrid RANS-LES Modelling, pp. 147–156. Springer, Gdansk, Poland (2010)

[20] Gand, F., Brunet, V., Mancel, G.: Zonal Detached Eddy Simulation (ZDES) using turbulent inflow and high order schemes: Application to jet flows. In: Progress in Hybrid RANS-LES Modelling, pp. 141–152. Springer, College Station, A&M University, Texas, USA (2015)

[21] Chauvet, N., Deck, S., Jacquin, L.: Zonal Detached Eddy Simulation of a controlled propulsive jet. AIAA Journal **45**(10), 2458–2473 (2007)

[22] Pope, S.B.: Turbulent flows. IOP Publishing (2001)

[23] Daviller, G., Brebion, M., Xavier, P., Staffelbach, G., Müller, J.-D., Poinsot, T.: A mesh adaptation strategy to predict pressure losses in les of swirled flows. Flow, Turbulence and Combustion **99**(1), 93–118 (2017)

[24] Benard, P., Balarac, G., Moureau, V., Dobrzynski, C., Lartigue, G., d'Angelo, Y.: Mesh adaptation for large-eddy simulations in complex geometries. International Journal for Numerical Methods in Fluids **81**(12), 719–740 (2016)

[25] Chapelier, J.-B., De La Llave Plata, M., Renac, F., Lamballais, E.: Evaluation of a high-order discontinuous Galerkin method for the DNS of turbulent flows. Computers & Fluids **95**, 210–226 (2014)

[26] de la Llave Plata, M., Lamballais, E., Naddei, F.: On the performance of a high-order multiscale DG approach to LES at increasing Reynolds number. Computers & Fluids **194**, 104306 (2019)

[27] Bassi, F., Botti, L., Colombo, A., Crivellini, A., Franciolini, M., Ghidoni, A., Noventa, G.: A p-adaptive matrix-free discontinuous Galerkin method for the implicit LES of incompressible transitional flows. Flow, Turbulence and Combustion **105**(2), 437–470 (2020)

[28] Abbà, A., Recanati, A., Tugnoli, M., Bonaventura, L.: Dynamical p- adaptivity for LES of compressible flows in a high order DG framework. Journal of Computational Physics **420**, 109720 (2020)

[29] Mozaffari, S., Guilmineau, E., Visonneau, M., Wackers, J.: Average-based mesh adaptation for hybrid RANS/LES simulation of complex flows. Computers & Fluids, 105202 (2021)

[30] Kaennakham, S., Holdø, A., Lambert, C.: A new simple h-mesh adaptation algorithm for standard Smagorinsky LES: a first step of Taylor scale as a refinement variable. The International Journal of Multiphysics **4**(1), 33–50 (2010)

[31] Waters, J., Carrington, D., Pepper, D.W.: An adaptive finite element method with dynamic LES for turbulent reactive flows. Computational Thermal Sciences: An International Journal **8**(1) (2016)

[32] Toosi, S., Larsson, J.: Anisotropic grid-adaptation in large eddy simulations. Computers & Fluids **156**, 146–161 (2017)

[33] Loseille, A., Alauzet, F.: Continuous mesh framework part I: well-posed continuous interpolation error. SIAM Journal on Numerical Analysis **49**(1), 38–60 (2011)

[34] Frey, P.-J., Alauzet, F.: Anisotropic mesh adaptation for CFD computations. Computer Methods in Applied Mechanics and Engineering **194**(48-49), 5068–5082 (2005)

[35] Dapogny, C., Dobrzynski, C., Frey, P.: Three-dimensional adaptive domain remeshing, implicit domain meshing, and applications to free and moving boundary problems. Journal of Computational Physics **262**, 358–378 (2014)

[36] Bourasseau, S.: Contribution to a mesh refinement method based on the adjoint vector for the computation of aerodynamic outputs (PhD thesis). Université Nice Sophia Antipolis (2015)

[37] Sadaka, G., Rakotondrandisa, A., Tournier, P.-H., Luddens, F., Lothodé, C., Danaila, I.: Parallel finite-element codes for the simulation of two-dimensional and three-dimensional solid–liquid phase-change systems with natural convection. Computational Physics Communications **257**, 107492 (2020)

[38] Basile, F., Chapelier, J.-B., de la Llave Plata, M., Laraufie, R., Frey, P.: Unstructured h- and hp- adaptive strategies for discontinuous Galerkin methods based on a posteriori error estimation for compressible flows. Computers & Fluids, 105245 (2021)

[39] Chapelier, J.-B., Lodato, G.: A spectral-element dynamic model for the Large-Eddy simulation of turbulent flows. Journal of Computational Physics **321**, 279–302 (2016)

[40] Marcum, D.L., Alauzet, F.: Unstructured mesh generation using advancing layers and metric-based transition for viscous flowfields. In: 21st AIAA Computational Fluid Dynamics Conference, p. 2710 (2013)

[41] Antoniadis, A.F., Tsoutsanis, P., Drikakis, D.: Assessment of high-order finite volume methods on unstructured meshes for RANS solutions of aeronautical configurations. Computers & Fluids **146**, 86–104 (2017)

[42] Tomac, M., Eller, D.: Steps towards automated robust RANS meshing. In: 4th CEAS Air & Space Conference, 16-19 September 2013, Linköping, Sweden, pp. 114–123 (2013). Linköping University Electronic Press

[43] Dippold, V.F.: Generating a grid for unstructured rans simulations of jet flows. In: 2018 Fluid Dynamics Conference, p. 3223 (2018)

[44] Acoustic Reference Nozzle with Mach 0.97, Unheated Jet Flow. https://www.grc.nasa.gov/www/wind/valid/arn/index.html (Accessed: 2021-10-15)

[45] Zhu, M., Arroyo, C.P., Pouangué, A.F., Sanjosé, M., Moreau, S.: Isothermal and heated subsonic jet noise using large eddy simulations on unstructured grids. Computers & Fluids **171**, 166–192 (2018)

[46] Lorteau, M., De La Llave Plata, M., Couaillier, V.: Turbulent jet simulation using high-order DG methods for aeroacoustic analysis. International Journal of Heat and Fluid Flow **70**, 380–390 (2018)

[47] Chollet, J.-P., Lesieur, M.: Parameterization of small scales of three-dimensional isotropic turbulence utilizing spectral closures. Journal of Atmospheric Sciences **38**(12), 2747–2757 (1981)

[48] Lamballais, E., Métais, O., Lesieur, M.: Spectral-dynamic model for large-eddy simulations of turbulent rotating channel flow. Theoretical and computational fluid dynamics **12**(3), 149–177 (1998)

[49] Ffowcs Williams, J.E., Hawkings, D.L.: Sound generation by turbulence and surfaces in arbitrary motion. Philosophical Transactions of the Royal Society of London. Series A, Mathematical and Physical Sciences **264**(1151), 321–342 (1969)

[50] Gand, F., Huet, M., Le Garrec, T., Cléro, F.: Jet noise of a UHBR nozzle using ZDES: external boundary layer thickness and installation effects. In: 23rd AIAA/CEAS Aeroacoustics Conference, p. 3526 (2017)

[51] Paliath, U., Premasuthan, S.: Large eddy simulation for jet installation effects. In: 19th AIAA/CEAS Aeroacoustics Conference, p. 2137 (2013)

[52] Tyacke, J.C., Wang, Z.-N., Tucker, P.G.: LES–RANS of installed ultra-high-bypass-ratio coaxial jet aeroacoustics with flight stream. AIAA Journal **57**(3), 1215–1236 (2019)

[53] Uzun, A., Lyrintzis, A.S., Blaisdell, G.A.: Coupling of integral acoustics methods with LES for jet noise prediction. International Journal of Aeroacoustics **3**(4), 297–346 (2004)

[54] Xia, H., Karabasov, S., Tucker, P., Dowling, A., Hynes, T.: Hybrid RANS-LES Modelling of Chevron Nozzles with Prediction of Far Field Sound. In: 49th AIAA Aerospace Sciences Meeting Including the New Horizons Forum and Aerospace Exposition, p. 21 (2011)

[55] Mendez, S., Shoeybi, M., Lele, S., Moin, P.: On the use of the Ffowcs Williams-Hawkings equation to predict far-field jet noise from large-eddy simulations. International Journal of Aeroacoustics **12**(1-2), 1–20 (2013)

[56] Rahier, G., Huet, M., Prieur, J.: Additional terms for the use of Ffowcs Williams and Hawkings surface integrals in turbulent flows. Computers & Fluids **120**, 158–172 (2015)

[57] Naqavi, I.Z., Wang, Z.-N., Tucker, P.G., Mahak, M., Strange, P.: Far-field noise prediction for jets using large-eddy simulation and Ffowcs Williams–Hawkings method. International Journal of Aeroacoustics **15**(8), 757–780 (2016)

[58] Lorteau, M., Cléro, F., Vuillot, F.: Analysis of noise radiation mechanisms in hot subsonic jet from a validated large eddy simulation solution. Physics of Fluids **27**(7), 075108 (2015)

[59] Caraeni, M., Dai, Y., Caraeni, D.: Acoustic investigation of rod airfoil configuration with DES and FWH. In: 37th AIAA Fluid Dynamics Conference and Exhibit, p. 4106 (2007)

[60] Langtry, R., Gren, E., Larssen, J., Spalart, P.: Evaluation of Structured and Unstrucutred Grids for Detached Eddy Simulation of Flap Edge Noise. In: 15th AIAA/CEAS Aeroacoustics Conference (30th AIAA Aeroacoustics Conference), p. 3102 (2009)

[61] Dahan, J., O'Reilly, C., Efraimsson, G.: Numerical investigation of a realistic nose landing gear. In: 20th AIAA/CEAS Aeroacoustics Conference, p. 2077 (2014)

[62] Kholodov, P., Moreau, S.: Identification of Noise Sources in a Realistic

Turbofan Rotor Using Large Eddy Simulation. In: Acoustics, vol. 2, pp. 691–706 (2020). Multidisciplinary Digital Publishing Institute

[63] Liu, W., Kim, J.W., Zhang, X., Angland, D., Caruelle, B.: Landing-gear noise prediction using high-order finite difference schemes. Journal of Sound and Vibration **332**(14), 3517–3534 (2013)

[64] Leicht, T., Jägersküpper, J., Vollmer, D., Schwöppe, A., Hartmann, R., Fiedler, J., Schlauch, T.: DLR-Project Digital-X-Next Generation CFD Solver'Flucs'. CEAS Aeronautical Journal (2016)

[65] Cockburn, B.: Discontinuous Galerkin Methods for Convection-dominated Problems, pp. 69–224. Springer, ??? (1999)

[66] Bassi, F., Botti, L., Colombo, A., Di Pietro, D.A., Tesini, P.: On the flexibility of agglomeration based physical space discontinuous Galerkin discretizations. Journal of Computational Physics **231**(1), 45–65 (2012)

[67] Roe, P.L.: Approximate riemann solvers, parameter vectors, and difference schemes. Journal of Computational Physics **43**(2), 357–372 (1981)

[68] Harten, A., Hyman, J.M.: Self adjusting grid methods for one-dimensional hyperbolic conservation laws. Journal of Computational Physics **50**(2), 235–269 (1983)

[69] Bassi, F., Rebay, S.: A high-order accurate discontinuous finite element method for the numerical solution of the compressible Navier–Stokes equations. Journal of Computational Physics **131**(2), 267–279 (1997)

[70] Witherden, F.D., Vincent, P.E.: On the identification of symmetric quadrature rules for finite element methods. Computers & Mathematics with Applications **69**(10), 1232–1241 (2015)

[71] Spalart, P., Allmaras, S.: A one-equation turbulence model for aerodynamic flows. In: 30th Aerospace Sciences Meeting and Exhibit, p. 439 (1992)

[72] Allmaras, S.R., Johnson, F.T.: Modifications and clarifications for the implementation of the Spalart-Allmaras turbulence model. In: Seventh International Conference on Computational Fluid Dynamics (ICCFD7), pp. 1–11 (2012)

[73] Shur, M., Spalart, P., Strelets, M., Travin, A.: Detached-eddy simulation of an airfoil at high angle of attack. In: Engineering Turbulence Modelling and Experiments 4, pp. 669–678. Elsevier, ??? (1999)

[74] de la Llave Plata, M., Couaillier, V., Le Pape, M.-C.: On the use of a

high-order discontinuous galerkin method for dns and les of wall-bounded turbulence. Computers & Fluids **176**, 320–337 (2018)

[75] Colombo, A., Manzinali, G., Ghidoni, A., Noventa, G., Franciolini, M., Crivellini, A., Bassi, F.: A p-adaptive implicit discontinuous Galerkin method for the under-resolved simulation of compressible turbulent flows. In: 7nd European Conference on Computational Fluid Dynamics (2018)

[76] Naddei, F., de la Llave Plata, M., Couaillier, V., Coquel, F.: A comparison of refinement indicators for p-adaptive simulations of steady and unsteady flows using discontinuous Galerkin methods. Journal of Computational Physics **376**, 508–533 (2019)

[77] Bernard, P.-E., Chevaugeon, N., Legat, V., Deleersnijder, E., Remacle, J.-F.: High-order h-adaptive discontinuous Galerkin methods for ocean modelling. Ocean Dynamics **57**(2), 109–121 (2007)

[78] Lodato, G., Chapelier, J.-B.: Evaluation of the spectral element dynamic model for large-eddy simulation on unstructured, deformed meshes. Flow, Turbulence and Combustion **101**(2), 271–294 (2018)

[79] Brès, G.A., Jordan, P., Jaunet, V., Le Rallic, M., Cavalieri, A.V., Towne, A., Lele, S.K., Colonius, T., Schmidt, O.T.: Importance of the nozzle-exit boundary-layer state in subsonic turbulent jets. Journal of Fluid Mechanics **851**, 83–124 (2018)

[80] Gand, F., Huet, M.: On the generation of turbulent inflow for hybrid RANS/LES jet flow simulations. Computers & Fluids **216**, 104816 (2021)

[81] Neifeld, A., Boenke, D., Dierke, J., Ewert, R.: Jet noise prediction with Eddy relaxation source model. In: 21st AIAA/CEAS Aeroacoustics Conference, p. 2370 (2015)

[82] Basile, F., Chapelier, J.B., Laraufie, R., Frey, R.: hp-adaptive hybrid RANS/LES simulations for unstructured meshes with the discontinuous Galerkin method. In: AIAA SciTech 2022 Forum, p. 1207 (2022)

[83] Shur, M.L., Spalart, P.R., Strelets, M.K.: LES-based evaluation of a microjet noise reduction concept in static and flight conditions. Journal of Sound and Vibration **330**(17), 4083–4097 (2011)

[84] Gand, F.: Investigation of turbulence development in incompressible jets with zonal detached eddy simulation (ZDES) and synthetic turbulent inflow. International Journal of Heat and Fluid Flow **61**, 425–437 (2016)

[85] Beck, A.D., Bolemann, T., Flad, D., Frank, H., Gassner, G.J., Hindenlang, F., Munz, C.-D.: High-order discontinuous galerkin spectral element

methods for transitional and turbulent flow simulations. International Journal for Numerical Methods in Fluids **76**(8), 522–548 (2014)

[86] Fehn, N., Wall, W.A., Kronbichler, M.: Robust and efficient discontinuous galerkin methods for under-resolved turbulent incompressible flows. Journal of Computational Physics **372**, 667–693 (2018)

[87] Krank, B., Kronbichler, M., Wall, W.A.: Direct numerical simulation of flow over periodic hills up to re h= 10, 595 \text {Re} _ {H}= 10 {,} 595. Flow, turbulence and combustion **101**(2), 521–551 (2018)

[88] Beck, A., Flad, D., Munz, C.-D.: Deep neural networks for data-driven les closure models. Journal of Computational Physics **398**, 108910 (2019)

[89] Bogey, C.: Grid sensitivity of flow field and noise of high-reynolds-number jets computed by large-eddy simulation. International Journal of Aeroacoustics **17**(4-5), 399–424 (2018)

[90] Welch, P.: The use of fast Fourier transform for the estimation of power spectra: a method based on time averaging over short, modified periodograms. IEEE Transactions on audio and electroacoustics **15**(2), 70–73 (1967)